

Exploring bound states of NbSe₂ van der Waals superconductor probed by tunneling spectroscopy

Inauguraldissertation

zur
Erlangung der Würde eines Doktors der Philosophie
vorgelegt der
Philosophisch-Naturwissenschaftlichen Fakultät
der Universität Basel

von

Zarina Mingazheva

Basel, 2024

Genehmigt von der Philosophisch-Naturwissenschaftlichen Fakultät
auf Antrag von
Erstbetreuer: Prof. Dr. Christian Schönenberger
Zweitbetreuer: Prof. Dr. Ernst Meyer
Externer: Dr. Oliver Gröning

Basel, 21. Februar 2023

Prof. Dr. Marcel Mayor
Dekan

Contents

1	Introduction	1
2	Theoretical background	3
2.1	A quantum dot coupled to a superconductor	4
2.1.1	Superconductors	4
2.1.2	Quantum dot	6
2.1.3	N-QD-SC devices	7
2.1.4	Andreev bound states in N-QD-SC devices	8
2.1.5	Ground states of the quantum dot strongly coupled to the SC	10
2.2	Tunneling spectroscopy	12
2.3	van der Waals materials	16
3	Device fabrication and measurement set-up	21
3.1	Device fabrication	22
3.1.1	Mechanical exfoliation	22
3.1.2	Forming a heterostructure by dry stacking technique	27
3.1.3	Fabrication of contacts to the stack	30
3.2	Cryogenics	30
3.3	Measurement set-up	33
3.4	Magnetic measurement and data processing	35
4	Characterisation of NbSe₂	37
4.1	Characterisation of macroscopic parameters of NbSe ₂ flake	38
4.1.1	Test device and measurement set-up	38
4.1.2	Critical current density j_c and critical temperature T_c	38
4.1.3	Magnetic characterisation of NbSe ₂	39
4.2	Superconducting gap of NbSe ₂ and its fitting	41
4.2.1	Quality of the tunnel junctions	42
4.2.2	Fitting of the superconducting energy gap	43
4.3	Summary	46
5	Subgap states in NbSe₂-MoS₂ heterostructures	49
5.1	Introduction	50
5.2	Results and discussion	51
5.3	Conclusion	55

5.4	Supporting information	56
5.4.1	Additional subgap spectres	56
5.4.2	Temperature dependence of the tunnel spectra	56
5.4.3	Device details	56
5.4.1	Alignment of the magnetic field for the tunnel junctions with sub-gap excitations	63
6	Conclusion and outlook	65
7	Appendix	67
7.1	Exfoliation	67
7.1.1	Material sources	67
7.1.2	Stacking	67
7.2	Fabrication contacts by electron beam lithography	67
	Bibliography	69
	Curriculum Vitae	77
	Publications	79
	Acknowledgements	81

1 Introduction

The advancement of solid-state electronics in recent years has been exceptionally remarkable, with the progress made in just the past 75 years since the invention of the transistor. The progress of electronics has made many things possible, such as powerful wireless smartphones and the World Wide Web. The continued progress, such as understanding the human body through genetic analysis or optimizing traffic flow with increasing numbers of cars, requires advanced computation. Classical computing based on the bit reached a very high performance. However, classical computers are slow for tasks that require high computational power, and their potential is limited because the thermal heating of transistors does not allow packing the transistors much closer. One solution to this issue could be quantum computing.

In a quantum computer, the basic unit is a qubit, which presents a quantum two energy - levels system. The main difference between the qubit and the bit is that qubits employ quantum entanglement, giving not only 0 and 1 states but the superposition of the states. This enables quantum computers to perform complex calculations more quickly than classical computers [1].

The materials that are often used to realize qubits are superconductors. These materials below some temperature conduct current without dissipation, but additionally, the ground state of the superconductor presents a macroscopic coherent condensate. In this thesis, we will be utilizing two-dimensional (2D) superconductors. Low dimensionality results in electron confinement in certain directions, leading to new properties, such as robustness to magnetic fields due to the lack of orbital effect. Furthermore, low dimensionality might lead to the formation of bound states, which could be utilized in qubits[2].

It is noteworthy that before the successful extracting of monolayer graphene from its bulk crystal by a technique known as mechanical exfoliation in 2004 [3], the existence of 2D materials was in doubt due to their predicted thermodynamical instability[4]. Nowadays, many 2D materials have been discovered, which have weak van der Waals forces between the layers and exhibit different electrical properties, from being an insulator to a superconductor[5].

In this thesis, I focus on one of such 2D material, superconducting NbSe₂. In addition to van der Waals coupling between layers, this material belongs to the group of transition metal dichalcogenides, where Nb is the transition metal, and Se is the chalcogen. Due to the presence of heavy transition metals,

this group of materials has strong-spin orbit coupling.

One can obtain heterostructures with perfect interfaces by stacking van der Waals materials together. In this thesis, we imply this property to engineer high-quality tunnel junctions. Tunneling spectroscopy is a well-known technique to characterize materials by probing their density of states. In addition to the superconducting energy gap of NbSe₂, we observe some sub-gap states that we assume are bound states formed due to the naturally formed quantum dot-like defects in tunnel junctions. This thesis focuses on studying the origin of these states.

Outline of the thesis

The thesis is organized in the following way. Chapter 2 discusses the theoretical backgrounds of superconductors (SC), quantum dots (QD), and hybrid QD-SC devices, including the concept of forming Andreev bound states. Furthermore, Chapter 2 covers the tunneling spectroscopy technique and the properties of van der Waals materials, specifically superconducting NbSe₂. Chapter 3 describes the device fabrication and measurement set-up, including the use of mechanical exfoliation and the dry stacking technique to form heterostructures, as well as the cryogenics and measurement set-up used in the study. Chapter 4 characterizes the macroscopic properties of NbSe₂, including the critical transition temperature and critical magnetic field values. We also provide the tunneling spectra of NbSe₂ and its fitting to investigate the nature of superconductivity in NbSe₂. Finally, Chapter 5 presents the results and discussion of subgap states in tunnel junctions based on NbSe₂.

2 Theoretical background

This chapter presents the theoretical background for the study of bound states formed in van der Waals tunneling devices. These bound states are treated as quantum dots that are connected to a superconductor. Therefore, the chapter covers the concepts of superconductivity, the properties of quantum dots, and the transport in hybrid devices composed of quantum dots and superconductors. A particular focus is placed on the formation of Andreev bound states and their ground state. Additionally, the chapter discusses tunneling spectroscopy as a technique for studying the density of states, and examines materials with van der Waals coupling between layers, specifically focusing on the superconductivity of NbSe₂.

2.1 A quantum dot coupled to a superconductor

In this section, we consider the transport of hybrid devices composed of a quantum dot (QD) and a superconductor (SC). The QD is similar to an atom, as it is a small conducting island that confines electrons in all three dimensions. This allows for the observation of single-electron transitions. Superconductors exhibit Cooper pairs transport. New phenomena may occur when the coupling strength between the QD and SC is the dominant energy scale in the system. In this section, we focus on the case where the superconducting gap is large compared to the charging energy of the QD, which disconnects the QD from the quasiparticles of the superconductor. By solving the Hamiltonian of the system, it was shown that the coupling between the SC and QD leads to the hybridization of the QD's even charge states, forming new energy levels called Andreev bound states. This enables the transport of Cooper pairs through the QD.

2.1.1 Superconductors

Superconductors are exotic materials, which below some specific temperature, called the critical temperature, lose their electrical resistivity¹. This phenomenon was discovered by Onnes in 1911, after the technological progress in obtaining liquid helium[6]. It was later found that a superconductor can conduct charge without dissipation due to electrons forming a coherent shared ground state². The ground state is known as the superconducting condensate and is separated from the excited states by an energy gap [7, 8].

The microscopic theory describing the phenomena of superconductivity was proposed by Bardeen, Cooper and Schrieffer [9], which is also known by its abbreviation BCS theory. This theory explains superconductivity as a phenomenon that occurs due to the formation of an effective attractive interaction between electrons near the Fermi surface.

In an intuitive picture, an electron moving in a lattice of positively charged ions creates a force, that is slightly displaces ions toward the electron. This creates a local place of increased positive charge density, and as a result another electron is attracted to this region [10]. It was also shown, that the binding energy and, therefore, the attractive interaction of the electron pair is maximum when the electrons have opposite momentum, i.e. $k_1 = -k_2$, where k_1 and k_2 are the electrons wavevectors [11, 12]. Furthermore, in the BCS theory, it is shown that electrons in a superconductor form spin singlet Cooper pairs³, i.e the total spin of Cooper pair is zero. Therefore, both electrons in the

¹At least up to 14 desimels

²Superconductivity is a truly macroscopic quantum phenomena.

³If Cooper pairs would have a total spin other than zero, this would lead to characteristic magnetic properties that are not detected for superconductors described by the BCS

pair have opposite spins[14]. Cooper pairs form the collective many-particle condensate, a singlet ground state of a superconductor [11].

The energy gap

The BCS theory also predicts an energy gap, by showing that to break a Cooper pair into two unpaired electrons also referred to as quasiparticles, the system needs an energy of $2\Delta(T)$, where $\Delta(T)$ is the so-called energy gap. The ground states and quasiparticles are separated by the energy gap. The quasiparticle density of states (DOS_q) was calculated to be equal to [11, 15]:

$$DOS_q = \begin{cases} DOS_n(E_F) \frac{|E-E_F|}{\sqrt{(E-E_F)^2 - \Delta^2}}, & (|E - E_F| > \Delta) \\ 0, & |E - E_F| < 0 \end{cases}, \quad (2.1)$$

where a particle's DOS in the normal state is $[DOS]_n$, while its energy is E . E_F is the Fermi energy, which lies in the middle of the gap of $2\Delta(T)$ for the superconductor.

When the temperature rises, the temperature broadening causes the smearing of the density of states and a decrease in the energy gap (Δ). When the temperature is greater than the critical temperature ($T > T_c$), the density of states becomes identical to that of the normal state. The temperature dependence of the energy gap can be described as follows [11, 13]:

$$\Delta(T) \approx \Delta(0) \left(1 - \frac{T}{T_c}\right)^{1/2} \quad (2.2)$$

where $\Delta(0)$ is the energy gap size at $T = 0$ and relates to the critical transition temperature as follows: [11]:

$$\Delta(0) \approx 1.74k_B T_c \quad (2.3)$$

Effect of an external magnetic field

In 1933, Meissner and Ochsenfeld showed that a material exhibits perfect diamagnetism in the superconducting state, thereby excluding magnetic fields[16]. However, the Gibbs energy of a superconductor increases with the applied magnetic field, whereas for a normal state, it remains relatively constant[7]. As a result, superconductivity can no longer be observed above a specific critical magnetic field.

According to how superconductivity breaks down under an external magnetic field, materials are divided into two types: type I and type II. In type I superconductors, there is a single critical field strength, $H_c(T)$, at which the material has a transition to the normal state. Type II superconductors present

theory[13]

the emergence of two critical fields, $H_{c1}(T)$ and $H_{c2}(T)$. Above $H_{c1}(T)$, the materials experience the formation of vortex cores, which present local normal states and, therefore, create a mixed state of normal and superconducting states. With the increase of the magnetic field, the number of vortices increases and eventually, at $H_{c2}(T)$, leads to the complete transition of the superconductor to the normal state.

The way superconductivity is broken in low-dimensional materials is affected by the confinement of electrons. For example, in the case of thin superconducting films, when a magnetic field is applied in-plane, the film's superconductivity is protected from the orbital effects, resulting in higher critical fields compared to bulk materials. However, superconductivity can be broken with the external magnetic field by Zeeman splitting when the splitting energy is equivalent or more than the gap energy, $\mu_B H \approx \Delta$, where μ_B is the Bohr magneton. This critical value is the Pauli paramagnetic limit (H_p), and by using Eq.2.3, one can obtain $H_p(T=0) = 1.86T_{c0}$ in the units of Tesla[17].

The BCS theory explains the properties of many superconductors, typically composed of metals or alloys. However, some superconductors are beyond this theory and referred to as unconventional superconductors. We will discuss one such material, namely NbSe₂, at the end of this Chapter and in Chapter4.

2.1.2 Quantum dot

A QD is a small conducting island, usually realized as a nanoscale semiconducting device, which confines electrons in all three spatial dimensions. As a result, the energy levels of electrons in the QD are discrete, like in an isolated atom. The level spacing, δE , depends on the QD's material and geometry parameters. Due to the small size of QDs and, therefore, the low capacitance C , the electron-electron interaction $U=e^2/C$ can not be neglected. It is often even the dominant energy scale at low temperatures [18].

The well-separated discrete energy levels are due to the QD being weakly coupled to the source and the drain via tunneling barriers[19], Fig.2.1(a). The coupling strengths are characterized by energy broadening parameters, Γ_{Source} and Γ_{Drain} , which are usually much less than U . Only due to recent technological progress, it became possible to make QD-SC devices with Γ_{Source} or $\Gamma_{Drain} \sim U$ [8].

One can add or remove an electron from the QD by applying a voltage capacitively to the QD (through the gate voltage V_g) and, therefore, change the electrochemical potential of the QD, Fig.2.1(a). When a small bias voltage ($\mu_S \approx \mu_D$) is applied between the source and the drain, and a QD energy level is tuned via the gate voltage V_g within the energy window defined by bias voltage, resonant tunneling transport will be observed as resonance peaks of dI/dV_{SD} as a function of the gate voltage[18], Fig.2.1(b-d).

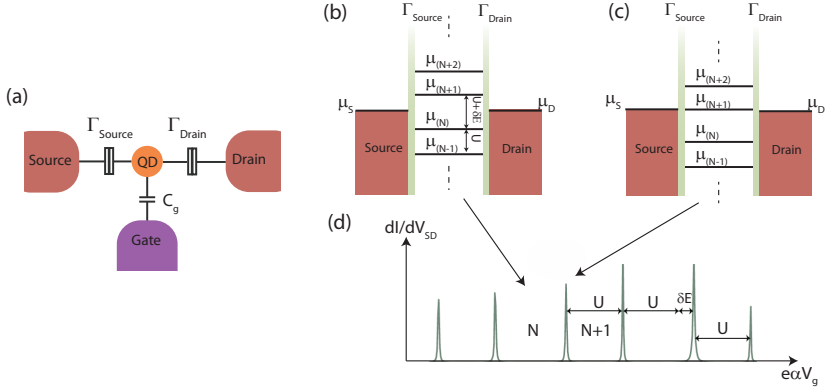


Figure 2.1 (a) The capacitor model of a QD connected to Source and Drain electrodes via tunnel coupling with $\Gamma_{Source/Drain}$ strength. The QD's electrostatic potential can be tuned by applying the voltage to the gate through the gate's capacitance C_g (a field effect). The alignment of the QD's electrochemical potential with respect to the source and drain can be either in a Coulomb blockade state (b) or in resonance (c). (d) Schematic of differential conductance resonance peak as a function of $e\alpha V_g$, where e is the electron charge, α is a lever arm ($\alpha = C_g/C$) and V_g is the gate voltage. The resulting current (and, therefore, conductance) can be measured when the QD energy level is tuned within the small energy window defined by V_{SD} . The plot is adapted from [20] and presented for the two-fold degenerated quantum dot.

2.1.3 N-QD-SC devices

In this section, we will consider the transport of Normal metal - QD - Superconductor structures, here and after abbreviated as N-QD-SC. The transport through such a system is determined by the strength of the following parameters: thermal broadening, spacing distance between levels of QD δE , the strength of charging energy U , coupling strength to the superconducting lead Γ_S , coupling strength to the normal lead Γ_N , and the size of the superconducting gap Δ [18]. The main references for this section are [19] and [21].

Quantum transport is typically studied at cryogenic temperatures, since high temperatures can cause thermal broadening which can wash out the results. Additionally, higher temperatures may lead to the appearance of thermal states [22] that are not relevant for the current discussion. For this reason, it is assumed in the following discussion that the effects of thermal broadening are negligible.

When Γ_N is large, such that $\Gamma_N \gg \Gamma_S$, and as long as the dot's energy level

is in the superconducting gap, there will be no tunneling of electrons from the QD to the superconductor due to weak coupling. Thus Andreev processes will be strongly suppressed. Therefore, in the following discussion we assume $\Gamma_N \ll \Gamma_S$.

When the charging energy is the most significant energy component, i.e., $U \gg \Gamma_S$, which means that the electron states of the QD are far away from each other, these states are robust to any hybridization. When $\Gamma_S \sim U$, the quantum dot and the superconductor are strongly coupled, leading to the formation of bound states. There are at least two types of bound states that might appear: Yu-Shiba-Rusinov states (YSR) and Andreev bound states (ABS). These states have similar features in the experiment results. However, the forming mechanisms are different. When the superconducting gap is small, the states are formed between electrons in the quantum dot and quasiparticles of the superconductor; these states are called YSR states. A large superconducting gap suppresses quasi-particles and therefore YSR states, but allows observing the formation of new energy levels of the QD called Andreev bound states [23, 24]. The ABS are formed due to the hybridization of even-charged states of the quantum dot mediated by the superconductor [23]. Thus, Cooper pairs between QD and SC can be transferred. Below we will focus only on the case of Andreev bound states.

2.1.4 Andreev bound states in N-QD-SC devices

When $\Gamma_S \sim U$ and Δ is large, the superconducting proximity effect significantly alters the QD's energy spectrum. The so-called superconducting Anderson model can be used to describe a QD-SC system. This model assumes a Hamiltonian in the following form [25]:

$$H_{tot} = H_{QD} + H_S + H_T, \quad (2.4)$$

where, a QD with a spin-degenerate single level orbit ϵ_d is taken and considered as follows:

$$H_{QD} = \sum_{\sigma} \epsilon_d d_{\sigma}^{\dagger} d_{\sigma} + U n_{\uparrow} n_{\downarrow}, \quad (2.5)$$

where $d_{\sigma}^{\dagger} (d_{\sigma})$ are the creation (annihilation) operators of the electrons with spin σ , and $n_{\sigma} = d_{\sigma}^{\dagger} d_{\sigma}$ the number operator of the QD. The second term describes the Coulomb interaction (U) of electrons in the QD and only takes place if both the spin up and spin down state of an energy level is occupied: $n_{\uparrow} = n_{\downarrow} = 1$ [19]. The BCS Hamiltonian describes the superconducting lead as follows:

$$H_S = \sum_{\mathbf{k}, \sigma} \epsilon_{\mathbf{k}} c_{\mathbf{k}\sigma}^{\dagger} c_{\mathbf{k}\sigma} - \Delta \sum_{\mathbf{k}} (c_{\mathbf{k}\uparrow}^{\dagger} c_{-\mathbf{k}\downarrow}^{\dagger} + \text{h.c.}), \quad (2.6)$$

where $c_{\mathbf{k}\sigma}^\dagger, (c_{\mathbf{k}\sigma})$ are the creation (annihilation) operators of the electron with spin σ , and wavevector \mathbf{k} and Δ is the superconducting energy gap.

The tunnel Hamiltonian describes a coupling between the superconducting lead and the QD as follows:

$$H_T = t_S \sum_{\mathbf{k}, \sigma} (d_\sigma^\dagger c_{\mathbf{k}, \sigma} + \text{h.c.}), \quad (2.7)$$

where the tunneling energy parameter, t_S , is related to the coupling strength, Γ_S , through the equation $\Gamma_S = 2\pi t_S^2 \rho_0$, where ρ_0 is a constant density of states in units of [1/eV] around the Fermi energy. In this model, only the superconducting lead is considered, and the second normal lead is not included.

Superconducting atomic limit

The Hamiltonian for the N-QD-SC system H_{tot} , Eq.2.4, can only be solved analytically under certain conditions. The simplest approximation to consider is the atomic limit. In this case, we assume that the tunneling coupling t_S is zero, so the lead and the QD are decoupled. The Hamiltonian of the isolated quantum dot, H_{QD} has four eigenstates: $\{|0\rangle, |\uparrow\rangle, |\downarrow\rangle, |\uparrow\downarrow\rangle\}$, Fig.2.2(a)[19]. The even-charge states $|0\rangle$ and $|\uparrow\downarrow\rangle$ with the total spin equals zero ($S=0$) are called singlets, and the odd-charge states $|\uparrow\rangle, |\downarrow\rangle$ with $S=1/2$, are called doublets.

The atomic limit described above does not allow to study of QD-SC systems. Therefore, to overcome this, researches have developed a concept of superconducting atomic limit, where the decoupling between the quantum dot and the quasiparticle continuum is achieved by taking the limit of a large superconducting gap, $\Delta \rightarrow \infty$ [19]. As a result, one could consider a local effective Hamiltonian [19, 21, 26] as follows:

$$H_{eff} = H_{QD} - \frac{\Gamma_S}{2} (d_\uparrow^\dagger d_\downarrow^\dagger + d_\uparrow d_\downarrow), \quad (2.8)$$

where the second term describes the proximity effect, which creates and annihilates Cooper pairs on the QD[19]. It arises due to the phenomenon of Cooper pair tunneling between a superconductor and the QD through a process called virtual Andreev process, which is enabled by the hybridization of the empty state $|0\rangle$ and the doubly occupied state $|\uparrow\downarrow\rangle$. The doublet states ($|\uparrow\rangle, |\downarrow\rangle$) remain eigenstates [21]. The eigenvalue of the doublet is considered to be exactly the middle between $E_{|0\rangle}$ and $E_{|\uparrow\downarrow\rangle}$ and, therefore, equal to $\epsilon_d + U/2$. This eigenenergy of the doublet we will denote as δ .

By comparing the local effective Hamiltonian, Eq.2.8, with the BCS Hamiltonian from Eq.2.6, it can be seen that the coupling constant Γ_S acts as the pairing energy 2Δ for the proximitied QD[19].

Due to the hybridization of even-charged states of the QD, they are no longer eigenstates of the QD. One can diagonalize the effective Hamiltonian to find new eigenstates using the Bogoliubov-de Gennes transformation as follows:

$$\begin{aligned} |S_{-}\rangle &= u|0\rangle - v^{*}|\uparrow\downarrow\rangle \\ |S_{+}\rangle &= v^{*}|0\rangle + u|\uparrow\downarrow\rangle, \end{aligned}$$

where u, v are the Bogoliubov-de Gennes amplitudes $u = 1/2\sqrt{1 + \delta/\sqrt{\delta^2 + \Gamma_S^2}}$ and $v = 1/2\sqrt{1 - \delta/\sqrt{\delta^2 + \Gamma_S^2}}$, where $\delta = \epsilon_d + U/2$ [19]. The resulting states $|S_{-}\rangle$ and $|S_{+}\rangle$ are Andreev Bound states with respective energies E_{-} and E_{+} , expressed as follows[19]:

$$E_{\pm} = \frac{U}{2} \pm \sqrt{\delta^2 + \Gamma_S^2} + \delta; \quad (2.9)$$

The resulting new eigenstates are illustrated in Fig.2.2 (c). Transitions that change parity by one, i.e., transitions of single electron tunneling with changing parity from odd to even or from even to odd, which are allowed in the QD, are $\{|\uparrow\rangle, |\downarrow\rangle\} \leftrightarrow |S_{-}\rangle$ and $\{|\uparrow\rangle, |\downarrow\rangle\} \leftrightarrow |S_{+}\rangle$. They are indicated by red arrows and the respective excitation energies are labelled as ζ_{-} and ζ_{+} .

These single-electron transition energies can be observed by tunneling spectroscopy in N-QD-SC devices with the QD weakly coupled to the normal electrode. In the conductance spectra, this would appear as subgap peaks at $eV_{SD} = \pm\zeta_{\pm}$. Chapter 5 presents our experimental results of such transitions.

2.1.5 Ground states of the quantum dot strongly coupled to the SC

As can be seen from the equation 2.9, the ground state of the quantum dot is the singlet $|S_{-}\rangle$ as long as $E_{-} < \delta$, and it is a doublet otherwise. The phase boundary condition (when $E_{-} = \delta$) can be easily derived from equation 2.9:

$$\frac{\delta^2}{U^2} + \frac{\Gamma_S^2}{U^2} = \frac{1}{4} \quad (2.10)$$

This presents a semicircle in the $(\frac{\delta}{U})$ - $(\frac{\Gamma_S}{U})$ -plane with the radius $1/2$ as illustrated in Fig.2.3. It is shown that the ground state is always singlet when Γ_S is a significant value (when the QD is strongly coupled to the superconductor). The horizontal axis of the graph represents the QD's electrochemical potential normalized by the QD's charging energy. By applying a gate voltage to the QD, it is possible to tune the electrochemical potential and observe the singlet to doublet transition.

An external magnetic field can also be used to observe the ground states transition. When the magnetic field is applied, the spins in the QD's doublet state will align either parallel or antiparallel to the field[19]. This causes the

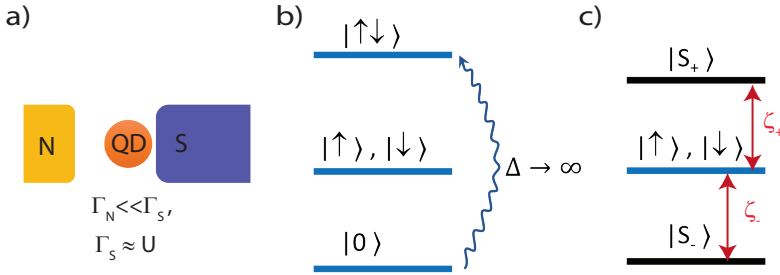


Figure 2.2 QD strongly coupled to a superconductor. The figure is adapted from [27]. (a) The schematic of N-QD-SC system when $\Gamma_N \ll \Gamma_S$ and $\Gamma_S \sim U$. (b) Energy spectrum of an isolated quantum dot with one spin-degenerate orbital. Suppose the dot is strongly coupled to the superconductor. In that case, the empty $|0\rangle$ and the doubly occupied states $|\uparrow\downarrow\rangle$ are hybridized via virtual Andreev processes (the blue arrow), which leads to the formation of new eigenstates [27]. (c) The energy spectrum of the QD-SC system in the superconducting atomic limit.

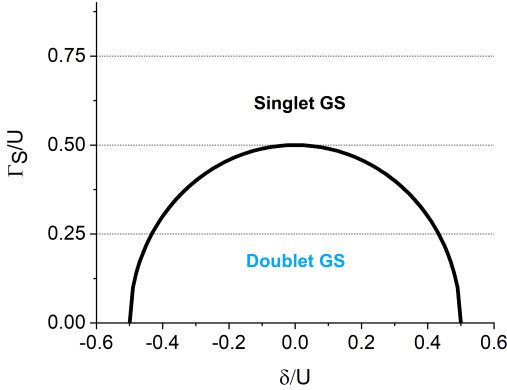


Figure 2.3 Phase diagram of the singlet and the doublet ground states as a function of $\frac{\delta}{U}$ and $\frac{\Gamma_S}{U}$ and approximation of the large superconducting gap, $\Delta \rightarrow \infty$. The figure is adapted from Ref. [21]

energy levels to be shifted proportionally to the field strength. This splitting between doublet's energy levels under the external magnetic field is known as the Zeeman effect and is determined by the effective g-factor of the quantum dot.

2.2 Tunneling spectroscopy

In this section, we will explore the concept of tunneling, a quantum phenomenon that allows for the movement of particles through high potential barriers. We will consider a system consisting of two conductors separated by an insulating barrier of high potential energy (U). The probability of an electron's location is represented by the square of its wave function. When an electron with energy less than the height of the potential barrier ($E < U$) attempts to move from one conductor to the other, its wave function decays exponentially as it passes through the barrier. However, if the width of the barrier is small enough, the wave function may not be fully suppressed, allowing for a non-zero probability of electron transport between the conductors.

Tunneling spectroscopy is an important technique in material science because it is a direct tool to study the electron's density of states of materials. The method was developed by Ivar Giaever in around 1960, who used it to confirm the energy gap in the superconductor's conduction band, which was predicted by BCS theory [28]. Below we discuss this method concerning our experiment, which are presented in Chapters 4 and 5.

Tunneling equation

In this section, we will derive the tunneling equation for a low-temperature tunneling experiment in which one of the conductors has a constant density of states. We will make several assumptions in this process, including the assumption that the tunneling is elastic (i.e., the energy of the electrons is conserved). Despite the simplicity of the system we are considering, the resulting tunneling equation is able to accurately describe a wide range of tunneling experiments. For a more comprehensive treatment of additional important parameters of tunneling experiments, such as thermal broadening, the reader is referred to [11].

Fig.2.4 (b) depicts the energy diagram of the tunneling process, consisting of two conductors separated by a thin insulating barrier. In this section, we will refer to the conductor with the higher chemical potential as the probe and the other as the sample. The transition probability of electrons through the insulating barrier depends on the characteristics of the barrier, which are captured in the "phenomenological" tunneling matrix element $|M|$. This matrix element is dependent on the width of the tunnel barrier and the work functions of the probe and the sample[11].

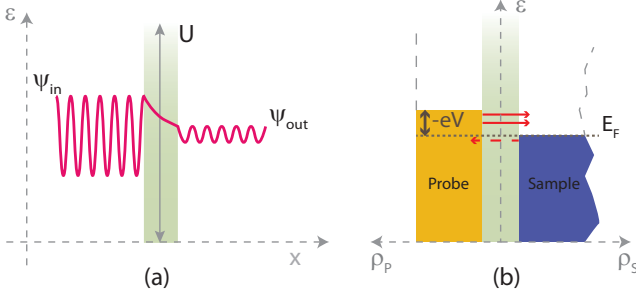


Figure 2.4 Tunneling process. (a) Exponential decay of the electron wavefunction, schematically represented as a sinusoidal wave packet, passes through the potential barrier; ψ_{in} and ψ_{out} indicate the wave function before and after the tunnel barrier, respectively. (b) The energy diagram of the tunneling process. The vertical axis represents energy, while the horizontal - is the density of states (DOS). The two conductors (named "Probe" and "Sample") are separated by the thin insulator - the high potential energy barrier (green). Here the probe is set at a higher chemical potential; the opposite is also possible. The difference between chemical potentials is eV . The current mainly goes from the conductor with the higher chemical potential to the lower, shown by pink arrows; however, at small eV , some current flows to the opposite side (the dashed pink arrow). The probe has constant DOS in the measuring range eV (the dashed grey line), and the sample has variable DOS.

To express the equation for the tunneling current, it is necessary to consider the occupied states of the probe, which in unit energy interval can be represented as the product of the probe's density of states and the Fermi-Dirac distribution for the probe [11]. We must also consider the free electron states of the sample, which are given by the product of the sample's density of states and $[1 - f(\epsilon)]$, the probability that the state at energy ϵ is empty, the equation 2.11. In order to account for currents flowing in the opposite direction, the equation 2.12 also considers the free states of the probe and the occupied states of the sample.

$$I_{P \rightarrow S} = A|M|^2 \int_{-\infty}^{\infty} (\rho_P(\epsilon - eV) \cdot f(\epsilon - eV)) \cdot (\rho_S(\epsilon) \cdot [1 - f(\epsilon)]) d\epsilon, \quad (2.11)$$

$$I_{S \rightarrow P} = A|M|^2 \int_{-\infty}^{\infty} (\rho_S(\epsilon) \cdot f(\epsilon)) \cdot (\rho_P(\epsilon - eV) \cdot [1 - f(\epsilon - eV)]) d\epsilon, \quad (2.12)$$

where A is the constant of proportionality, which includes geometric parameters of the conductors, electron charge, etc., $|M|$ is the tunneling matrix element, V is the applied voltage, eV is the difference in the chemical potentials between the probe and sample, $\rho_S(\varepsilon)$ and $\rho_P(\varepsilon - eV)$ are DOS of the sample and the probe respectively, and $f(\varepsilon)$ and $f(\varepsilon - eV)$ are Fermi-distribution functions for the sample and the probe respectively[11].

At the cryogenic temperatures at which we perform our measurements, the thermal broadening is negligible, therefore, the above integrals can be reduced to integrals from Fermi energy of the sample, E_F , to $E_F + eV$. The Fermi-Dirac distributions for the probe and the sample can also be treated as if they were at zero temperature. The effective current I is the subtraction of $I_{P \rightarrow S}$ and $I_{S \rightarrow P}$ and has a direction from the part with the higher chemical potential to the lower one. As a result, we obtain the following final equation for the current:

$$I = I_{P \rightarrow S} - I_{S \rightarrow P} = A|M|^2 \int_{E_F}^{E_F + eV} \rho_S(\varepsilon) \rho_P(\varepsilon - eV) d\varepsilon. \quad (2.13)$$

As previously mentioned, the material chosen for the probe is assumed to have a constant density of states in the measured range eV , such that $\rho_P(\varepsilon - eV) \approx \text{constant}$. This assumption holds true for many normal (non-superconducting) metals, such as gold and platinum.

To analyze the electron density of states of the sample, we take the derivative of equation 2.13. The first derivative of the tunneling current as a function of voltage is referred to as the tunneling differential conductance, which is often measured in experiments[11].

$$dI/dV \sim \rho_S(eV). \quad (2.14)$$

Tunneling of N-I-S system

It is possible to study the quasiparticle DOS of a superconductor (S) using tunneling devices, in which one conductor is a normal metal (N) with a constant density of states. These heterostructures, known as NIS tunnel junctions, are depicted in Fig.2.5, showing energy diagrams at different values of applied voltages compare to superconducting gap.

The tunneling experiment

In this work, we focused on characterizing NbSe₂, an air-sensitive superconducting van der Waals material, whose properties are described in Section 2.3. To study it, we employed a planar tunneling spectroscopy technique, in which a nano-thin insulator is placed between two electrodes. There are several reasons for choosing this method: (i) van der Waals (vdW) stacks are known to

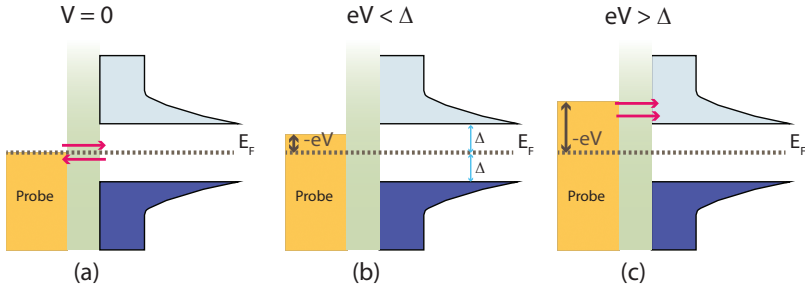


Figure 2.5 The energy diagrams of the NIS tunnel junction. The vertical direction represents energy, while the horizontal - is DOS. (a) At $V = 0$, the chemical potentials of the probe and the sample are aligned, and a non-zero probability for Cooper pair current exists in both directions. However, the effective current equals zero. (b) At small V , the resulting current is still zero because there are no single-particle states inside the superconducting gap. (c) When $eV \gtrsim \Delta$, the effective current $I > 0$.

have a perfect interface, so we used vdW dielectrics (such as 3 or 4 layers of MoS_2 or a bilayer of hBN) as the tunnel barrier; (ii) the insulator allowed us to encapsulate the air-sensitive NbSe_2 from the environment; and (iii) the planar tunneling heterostructure is a mechanically compact and stable device, which allows for measurements to be taken in any fridge and for multiple experiments to be performed on a single device.

One additional feature we get from our planar tunneling devices is an observation of inelastic tunneling channels, in which electrons lose a portion or all of their energy as they move from one electrode to the other. This energy can be transferred and excites other processes. Consider the case of tunneling through a quantum dot coupled to a superconductor. Such energy excites an electron in a quantum dot to a higher level.

One disadvantage of using planar tunneling spectroscopy compared to scanning tunneling microscopy is that it averages the measured tunneling conductance over the area of the tunnel junction. For example, in our experiments, we fabricate tunnel junctions with an area on the order of $1 \mu\text{m}^2$ to obtain large enough tunneling signals. This averaging limits the spatial resolution of the DOS measurements; however, despite this limitation, planar tunneling spectroscopy remains a useful tool for probing the properties of materials, particularly for cryogenic measurements.

2.3 van der Waals materials

In this section, we will examine the properties and characteristics of NbSe₂, MoS₂, and hBN, which are part of the van der Waals materials group. These materials are so named because they are held together by weak van der Waals forces between layers, while the atoms within the layers are bound by strong covalent bonds[5]. NbSe₂ and MoS₂ are also classified as transition metal dichalcogenides, and this subgroup of materials is known for its strong intrinsic spin-orbit coupling.

Superconducting NbSe₂

NbSe₂ is a superconductor that is known for the coexistence of charge density waves⁴ and superconductivity. According to research [30], this material preserves superconducting properties down to monolayers, with a critical temperature (T_c) of approximately $T_c \approx 3$ K, while for the bulk $T_c \approx 7$ K, Fig.2.6[30].

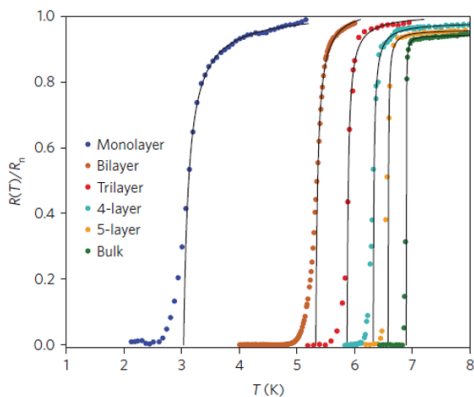


Figure 2.6 Resistance of NbSe₂ samples with different thicknesses as a function of the temperature. The resistance value is normalized to the normal state value. The experimental data is indicated by symbols, while the solid lines are provided fitting. Figures are adapted from Ref.[30].

As was mentioned above, NbSe₂ is a transition metal dichalcogenide (TMD). This group of materials has a structure in the form of MX₂, where M is a

⁴A charge density wave(CDW) is a periodic modulation of the distortion of the lattice or electron density conduction. To know more about CDW in NbSe₂, the reader might refer to [29].

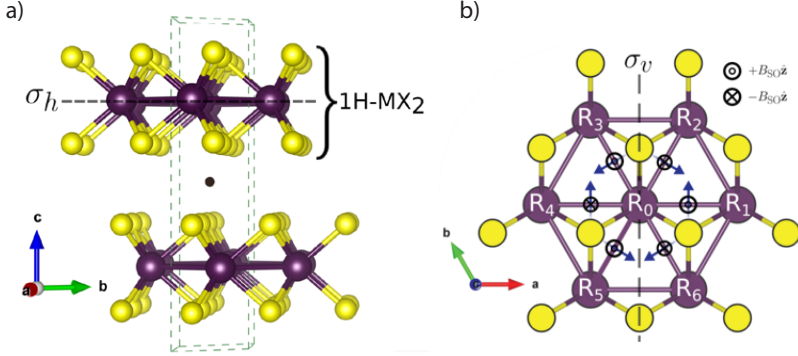


Figure 2.7 Crystal structure of 2H-MX₂ TMD. The transition metal M is shown in violet and the chalcogen X is shown in yellow. (a) Side view on the crystal structure. The unit cell of the 2H-MX₂ is shown by the dashed green line, the inversion center by the black dot. (b) Top view on the monolayer TMD (1H-MX₂). The structure has a basal mirror plane, and three perpendicular mirror planes, one of them indicated as σ_v . The crystal field directions indicated by the blue arrows, the antisymmetric Ising spin-orbit magnetic field B_{SO} also indicated by black circles with directions. Figures are adapted from Ref.[31].

transition metal (such as Mo or Nb), and X denotes to a chalcogen (such as S or Se)[31]. The transition metal layer is located between two layers of chalcogens, Fig.2.7(a).

One of the common crystal structures of TMD is the hexagonal polytype, 2H-MX₂. The inversion center of 2H-MX₂ is located between the layers, Fig. 2.7(a); therefore the odd layer TMD is non-centrosymmetric. This crystal structure provides out-of-plane mirror symmetry, which leads to the restriction of the crystal field (ε) to the in-plane of the layers, Fig. 2.7(b).

In TMD, the hybridization of the d orbitals of the heavy transition metal and the s orbital of the chalcogenide atoms lead to strong intrinsic spin-orbit coupling, which can be described as an intrinsic out-of plane magnetic field: $\mathbf{H}_{SO}(\mathbf{k}) \propto \mathbf{k} \times \varepsilon$, where \mathbf{k} is the crystal momentum [17, 30]. The broken inversion symmetry for the odd layers NbSe₂ allows for antisymmetric directions of the spin-orbit field in opposite corners of the hexagonal Brillouin zone, Fig.2.8(a)[32].

The large antisymmetric intrinsic \mathbf{H}_{SO} leads to Zeeman energy splitting

between spin states by a large spin-orbit gap⁵ (Δ_{SO}) and the spin splitting changes sign upon inversion through the Brillouin zone center[32], Fig.2.8(a). This leads that Cooper pairs mainly form between electrons of opposite valleys with opposite spin polarizations, known as the Ising pairing.

H_{SO} also pins spins of electrons in Cooper pairs and prevents their alignment when the in-plane magnetic field is applied, allowing for large upper critical magnetic field values[17]. As was shown above in Sec.2.1.1, for BCS two-dimensional materials, the upper critical magnetic field is given by the Pauli limit. It was proved experimentally that in monolayer Ising superconductors, such as NbSe₂ or TaS₂ the upper critical magnetic field is larger than the Pauli limit (H_p) [30, 32], Fig.2.8 (b-c) and can be estimated as $H_{c2}^{\parallel} \sim \sqrt{H_{SO}H_p}$ [32].

It was also observed experimentally that for bilayer NbSe₂, when the inversion symmetry is restored, the H_{c2}^{\parallel} is larger than the Pauli limit and in general, no oscillation of the upper critical magnetic field occurs with the layer number[30, 32], Fig.2.8(b). This can be explained by weak coupling between the layers[32]. If there is no interlayer coupling, this would be equivalent to the monolayer Ising superconductor. As was shown in [32], a small amount of tunneling happens in neighboring layers between d orbitals of Nb atoms. The crystal field is inverted in the neighboring layers, leading to the opposite effective field, Fig.2.8(d). It was shown that interlayer hopping is small compared to Δ_{SO} , however increase with number of layers, Fig.2.8(e), which leads in decreasing of the upper critical magnetic field with the layer numbers[32].

Insulating MoS₂ and hBN

Two other materials that we employed in our project are 2H-MoS₂ and hBN. These materials have interesting properties and are actively used in many other types of research, for example, in electronic transport [33, 34], and optics [35]. Here we outline only the dielectric properties of 2H-MoS₂ and hBN since we use them as the tunnel barriers.

MoS₂ is a semiconducting TMD. The band gap in the bulk is 1.29 eV [36]. When the number of layers is decreased, the bandgap reaches 1.9 eV for the monolayer[36]. The Fermi level in this material is naturally pinned relatively close to the minimum of the conductance band, as indicated by the red dashed line on the band structure in Fig.2.9(a). As a result, it can become conductive when a gate voltage is applied. Like NbSe₂, MoS₂ also exhibits strong spin-orbit coupling due to the presence of a transition metal.

Hexagonal Boron Nitride (hBN) has a crystal structure similar to graphite, with a hexagonal lattice composed of two different atoms (boron and nitrogen) in its unit cell[37]. hBN is an insulator with a large bandgap of around 5.9

⁵For example, for 2L NbSe₂, the Fermi surface average $\Delta_{SO} \approx 50meV$ while for comparison, the superconducting gap is around 1 meV[32]

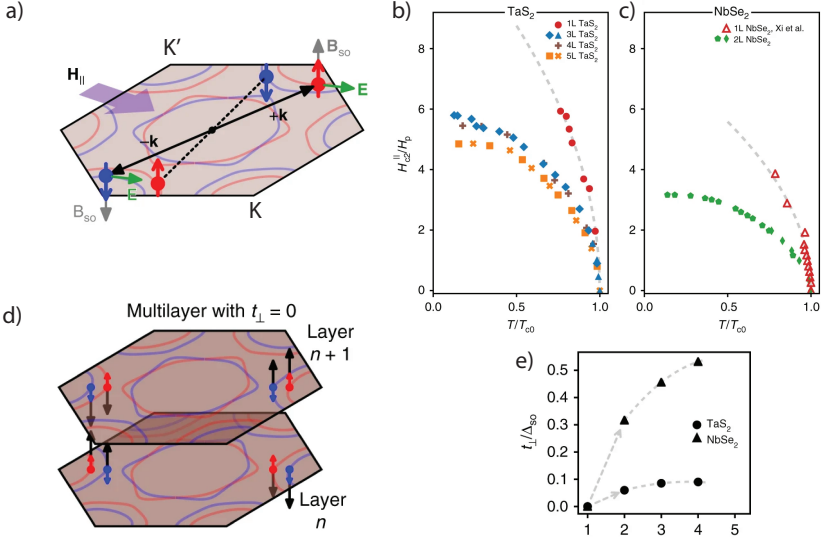


Figure 2.8 a) Schematic Fermi surface with spin projections for monolayer Ising superconductor. By red is shown one projection of the spin (for example, "up"), while by blue shows the opposite projection (for example, "down"). The spin splitting is maximum in K and K' valleys. Grey arrows indicate the antisymmetric spin-orbit field directions. Such spin-splitting leads that Cooper pairs mainly form between electrons in the opposite valleys, as indicated by black solid and black dashed arrows. As a purple arrow, the external in-plane magnetic field is indicated. b) Parallel upper critical magnetic field for TaS₂ samples with different thicknesses as a function of the transition temperature. The magnetic field value is normalized to the Pauli limit. c) Parallel upper critical magnetic field for NbSe₂ d) Schematic Fermi surface for multilayer NbSe₂. The interlayer coupling is set to zero ($t_{\perp}=0$). By red and blue arrows indicated opposite spin projections. It is shown opposite B_{SO} in surrounding layers because of crystal field inversion between layers. e) The value of interlayer coupling energies (t) normalized to the spin-orbit gap as a function of the number of layers. The ratio is obtained from the density functional theory calculation. The dashed line is a guide to the eye. Figures are adapted from Ref.[32]

eV. The Fermi level is naturally pinned close to the center of the band gap, as shown in Figure 1.11(b)[37].

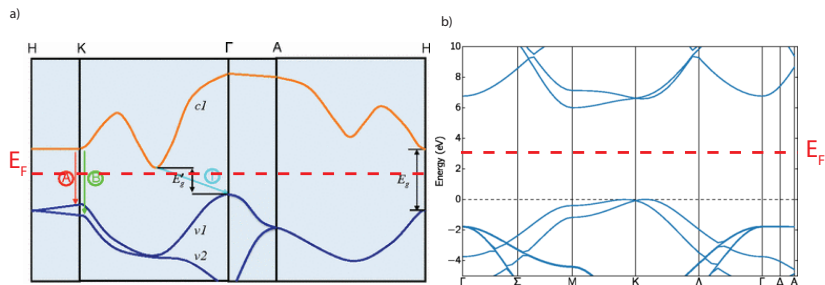


Figure 2.9 a) The simplified band structure of bulk MoS₂, showing the highest split valence bands $v1$ and $v2$ and the lowest conduction band $c1$. By E_g' , the indirect band gap for the bulk MoS₂ is indicated. Monolayer MoS₂ is become a direct band insulator with bandgap E_g [36]. Fermi level is pinned close to the minimum of conductance band as we indicated by red dashed line. b) The calculated band structure of bulk hBN. The zero of the energy axis is taken the maximum of the valence band[37]. hBN has a large band gap with Fermi level around the middle of the gap, as we indicated by the red dashed line. Fig. a) is adapted from Ref. [36] and b) from Ref.[37]

3 Device fabrication and measurement set-up

In order to investigate quantum phenomena such as tunneling and electron transport in nanostructures, it is necessary to utilize high-quality devices. However, the fabrication of these devices can be challenging due to the sensitivity and dependence on numerous parameters at the nanoscale. This chapter describes the basic process for fabricating van der Waals tunneling devices based on NbSe₂. The fabrication recipes can be found in appendix 7. The chapter closes with brief descriptions of the measurement set-up and data analysis process used for magnetic measurements.

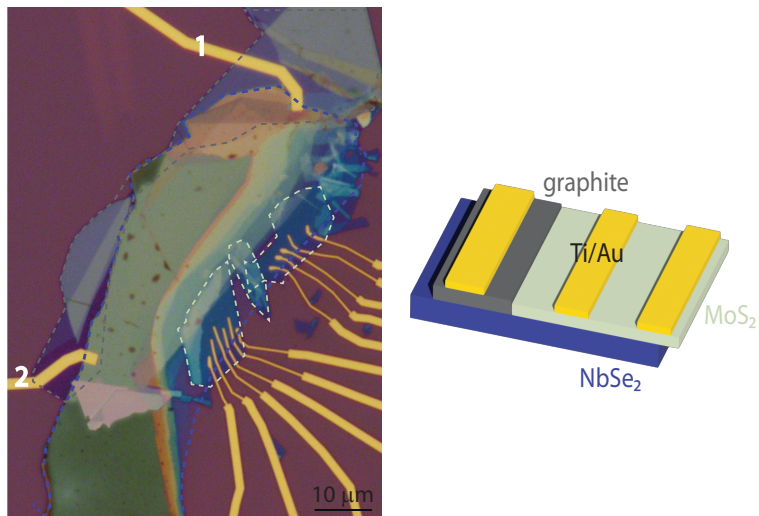


Figure 3.1 The optical image of the NbSe₂-MoS₂-Ti/Au tunnel junction device and the corresponding schematic. Colors on the dashed contours correspond to colors on the schematic on the right. The graphite flake was used to make good contact to NbSe₂. Electrodes 1 and 2 are the electrodes to the superconductor, while the other electrodes on the right side serve as tunnel junctions fabricated on top of MoS₂.

3.1 Device fabrication

In this section we describe the fabrication process used for the devices presented in this thesis. The process begins with obtaining high-quality flakes by mechanical exfoliation. These flakes are then assembled into a heterostructure, using a dry transfer technique.

3.1.1 Mechanical exfoliation

Successful isolation of monocrystalline few atomic layer graphene and demonstration of its promises for future electronics opened the path for active investigation of van der Waals materials [3, 38, 39]. Mechanical exfoliation is a technique that allows for the isolation of few-atomic layers and even single-layer crystals from their bulk materials [3]. This method utilizes the well-known tendency of crystals to split along the plane with weaker bonds, called

cleavage. And therefore, in combination with the approach of using adhesive tape, mechanical exfoliation appears very effective for van der Waals materials, materials with weak van der Waals bonds between layers. In our study we followed the below process for the mechanical exfoliation^[15]

1. The adhesive tape and crystal are taken, Fig.3.2(a). The crystal is put in good contact with the tape and then detached so that we have a footprint of the crystal on the tape, Fig.3.2(b).
2. This footprint is then duplicated until the tape is covered by the crystal's flakes with a high density, Fig.3.2(c, d). However, it is critical that the flakes do not overlap¹. Such a tape with flakes is usually called the "master" tape and can be used for many exfoliation processes.
3. A clean adhesive tape needs to be taken and put in good contact with the master tape² and gently detached, taking care to obtain ideally only freshly cleaved crystals onto the clean tape (here and after the copy tape).
4. The clean pre-cut silicon substrates³ are put in good contact with the copy tape, Fig.3.2(e) and then detached so that ideally only fresh cleaved flakes are extracted on the substrates. After this, the flakes on the substrates are analyzed under an optical microscope.

For the case of air-sensitive materials, such as NbSe₂, the mechanical exfoliation needs to be done in an inert atmosphere, for example, in a glove box. For our project, we used the glove box from MBraun Inertgas-Systeme GmbH operated in an inert nitrogen atmosphere with oxygen and water concentrations of less than one particle per million (<1 ppm) nitrogen particles, Fig. 3.5 (a). In the next step of forming a heterostructure, air-sensitive materials are usually encapsulated with other materials, protecting them from oxidation outside the glove box.

General criteria for the flakes and a thickness analysis

Desired flakes should meet specific criteria on the following parameters: (i) thickness, (ii) lateral size, and (iii) cleanliness and absence of defects.

In the case of tunneling spectroscopy, it is essential to have an optimal thickness tunnel barrier, in our case MoS₂ or hBN. One common approach to analyze the flake's thickness is to measure its optical reflectivity contrast.

¹Some sources suggest that it is good to make a copy of the crystal no more than ten times [15]

²We usually press them together slightly for around 60 seconds

³The humidity from the top of the silicon substrates needs to be removed. For this, one can heat the substrates more than 100°C to evaporate water, then cool them down for several seconds to avoid damaging the adhesive tape. One can also clean the surface with plasma to increase the adhesion of the substrate's surface, for example, by using oxygen plasma for around 20 seconds



Figure 3.2 Mechanical exfoliation process. (a) The bulk crystal with the size of around $1\text{ cm} \times \text{cm}$ and the adhesive tape. (b) The bulk crystal was put in close contact by folding the tape and then detached from it, such that we have two footprints of the crystal (c) The footprints are duplicated by folding the tape (d) The density of flakes increased by folding the tape more times. (e) The silicon substrates put in good contact with the copy tape.

To enhance the contrast between flake and the substrate, silicon oxide is grown with the desired thickness on Si wafer [40], Fig. 3.3 (a). The metals and semiconductors, such as MoS_2 , have good optical contrast and, therefore, can be successfully exfoliated onto a commonly used substrate with 285 nm of SiO_2 .

For hBN, which has a very wide bandgap of around 5.9 eV we use 90 nm SiO_2 that gives the best contrast as shown in [40]. The contrast values depend also on the intensity of the light source. Below we consider the contrast values for the optical microscopic image of MoS_2 flake captured by a Nikon DS-Ri2 with the light source Nikon Intenslight C-HGFI and a 100x objective. The optical image is split into red, green, and blue channels using the open-source software ImageJ, Fig. 3.3 (b). Each pixel's intensity has been rescaled using 256 gray levels, with 0 being the darkest and 255 being the brightest with ImageJ, Fig. 3.3 (c). For each color channel, one can calculate the optical contrast (C) as a relative intensity (I) ratio between the analyzed flake's region and background by the following equation:

$$C_{\text{flake}} = \frac{I_{\text{flake}} - I_{\text{bcg}}}{I_{\text{bcg}}} \cdot 100\%,$$

where I_{flake} and I_{bcg} are intensity of the reflected light from the flake and

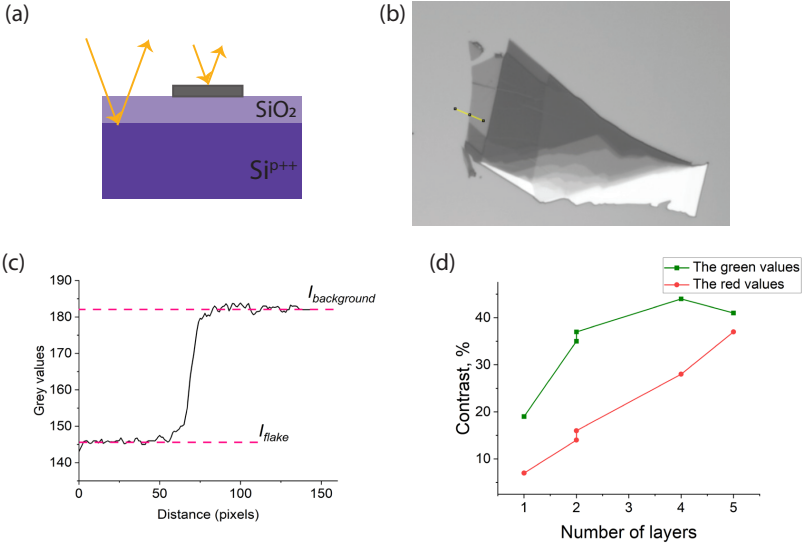


Figure 3.3 The thickness analysis of the flakes by the optical reflectivity contrast approach. (a) The SiO₂ layer is grown on the top of the Si wafer to enhance interference. In the schematic we did not account refractions of the lights. (b) An optical image of MoS₂ flake split into different channels (here the green channel is shown). (c) Rescaled values of the reflected light intensity of the flake I_{flake} and background I_{bcg} for the part of the flake shown in (b) by the yellow line. (d) The whole analysis of this MoS₂ flake for the green and the red channels. The blue channel gives much smaller contrast values and, therefore, is not considered here.

substrate respectively.

As mentioned above, the contrast values significantly depend on the thickness of SiO₂ which varies in practice and gives different contrasts. Therefore, it is good to study optical contrast for the flakes with a similar background as the desired flake. For example, if we look for a 4-layer MoS₂ flake, we should also study the optical contrast of 1-layer, 2-layer, 3-layer, and 5-layer flakes with the same background to ensure that the candidate is indeed a 4-layer flake. We often notice that the optical contrast of MoS₂ in the green channel begins to saturate and decreases for flakes with 4 layers or more, while the optical contrast in the red channel remains reliable and increases at least up to 5 layers, as shown in Figure 3.3(d).

Flakes with a good lateral size are necessary to provide a sufficient working

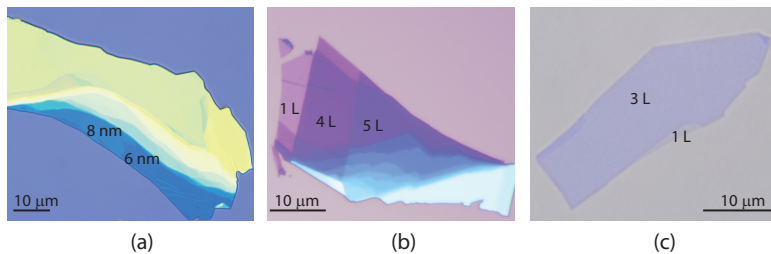


Figure 3.4 Exfoliations of two-dimensional materials. The materials exfoliated onto p-type Si wafers with a grown SiO_2 top layer enhancing the contrast. (a) The NbSe_2 flake on Si wafer with 285 nm of SiO_2 . The flake has regions with 6 nm and 8 nm thicknesses, and some thicker ones that appear yellow. (b) MoS_2 flake on Si wafer with 285 nm of SiO_2 . The flake has a monolayer (1L), four-layer (4 L), five-layer regions (5 L), and other thicker part. However, the flake is far from good due to the small 4 L part and crystal's folds. The background colors for (a) and (b) are different. This is due to the non-uniform SiO_2 thickness at the edge of the wafer. (c) hBN flake on Si wafer with 90 nm of SiO_2 . It is shown that the optical contrast is better on Si wafer with 90 nm SiO_2 [40]. The flake has monolayer (1 L) and three-layer (3 L) parts.

area for the device. For our tunneling spectroscopy devices, we typically choose flakes that allow us to fabricate more than ten tunnel junctions. The properties of materials can also vary depending on the crystal direction, so for certain projects, the crystal direction of the flake is also important.

A clean flake is essential for a good device. Adhesive tape often leaves residues, other defects are cracks and folds of flakes. Both kinds of defects are possible to see in the dark field mode of the optical microscope⁴ or with AFM.

Fig.3.4 shows examples of flakes that were used for tunneling devices in our study. We mainly worked with NbSe_2 flakes thicker than 5 nm, MoS_2 3-5 layers thick and 2-3 layers thick hBN. The advantage of mechanical exfoliation for vdW materials is that it allows us to easily obtain monocrystalline materials down to monolayers. The disadvantage of this method is the small lateral sizes of the flakes and the time-consuming process of analyzing flakes.

⁴For this, the microscope should have a powerful light source.

3.1.2 Forming a heterostructure by dry stacking technique

To make an electronic device with specific functions, it is often necessary to combine multiple materials with different characteristics. In the case of van der Waals devices, one needs to stack the flakes together into a heterostructure. There are several ways of stacking [41], we will focus on the dry transfer method developed by Wang et al.[42] and Zomer et al.[43].

Preparing transfer slides

To pick up flakes from the substrate in a highly controlled way, one can use a transfer slide consisting of a microscope slide with a system of adhesive polymers. The process of preparing transfer slides is as follows:

1. The cleaned with acetone and ultrasound polydimethylsiloxane (PDMS) is cut into small pieces. The size is chosen to be less than the diameter of a future polycarbonate (PC) window. One of the piece of PDMS is put into a clean microscope slide, this is a base for the transfer slide.
2. A thin PC film is deposited on a clean microscope slide by dripping the PC solution on the slide and spreading by a second microscope slide. After this, the slides are immediately separated, and, as a result, both microscope slides are covered by thin, uniform PC film.
3. The part of PC film is removed with an adhesive tape having a window in its center⁵, Fig.3.5 (b).
4. On top of the PDMS base, the adhesive tape with PC window is placed, Fig.3.5 (c).

After this, the transfer slide is mounted to the x-y-z manipulator and located above the substrate with the desired flake, Fig.3.5 (d). The clean, defect-free space in the PDMS/PC window of the transfer glass is used to make a stack.

Stacking process

Many combinations of van der Waals materials are possible. It is also possible to put flakes at any angle relative to each other. Fig.3.6 shows a simplified stacking process of NbSe₂-MoS₂ tunneling devices. During the stacking process, the transfer slide is kept at a small angle toward the substrate, usually less than 0.5 degrees. This helps ensure better contact with the desired flake while minimizing the pickup of surrounding flakes, which could be an issue for future fabrication of contacts to the stack.

First, the small graphite flake is picked up, it serves only for ohmic contact with NbSe₂. For this step, we increase the temperature of the microscope

⁵One of the ways to make such windows is by an office hole punch. For this, two pieces of adhesive tape are connected to each other, then the hole is made, and then they are separated

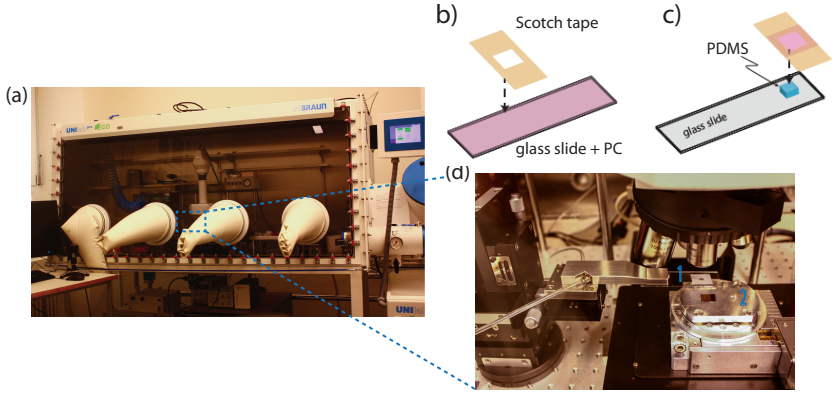


Figure 3.5 Set-ups for stacking. (a) The glove box allows to work in a nitrogen environment with O_2 and H_2O concentrations less than one ppm. (b) A glass slide is covered by PC (pink) and partly lift-off by an adhesive tape. (c) Clean PDMS pillow with the size around $4 \times 4 \text{ mm}^2$ on the glass slide is covered by suspended PC film. (b) and (c) show the process of preparing transfer slides, adapted from [15]. (d) Here is possible to see the transfer slide manipulator, a transfer slide (1), and the microscope stage with the laying substrate with the size around $1 \times 1 \text{ cm}^2$ (2). The whole stacking set-up is connected to a computer and manipulated by joysticks.

stage, where the substrate with the flake is located, to 80 degrees. Then, we bring the transfer slide into contact with the substrate until the desired flake is well-covered. After this, we wait for around three minutes and slowly pick up the transfer slide from the substrate. The second flake is 3-5 layers MoS_2 which we slightly overlap with graphite, Fig.3.6 (b). The procedure for picking up is the same, however, for the second flake it is possible to use a lower temperature because the second flake is likely to have a better connection to the flake on the transfer slide than to the substrate. Due to the difficulty in finding tunnel barrier flakes with precisely desired thickness and large lateral dimensions, we usually use several MoS_2 flakes of the desired thickness and put them next to each other to cover as much NbSe_2 as possible. Additionally, when we need to isolate the edges of NbSe_2 electrically, we use MoS_2 flakes that are thicker than 5L and place them over the edges of NbSe_2 . The process of picking up flakes is continued unless the whole assembly is ready.

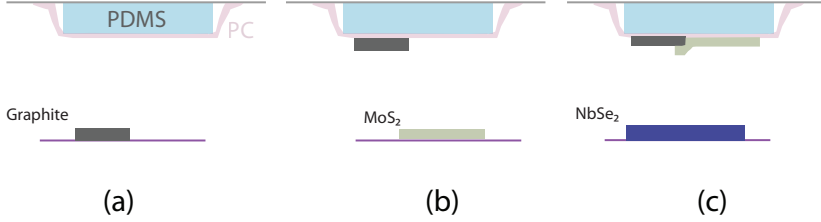


Figure 3.6 Simplified stacking process. (a) Picking up the first flake, which in our case is graphite. Transfer slide and flake are put in the contact and detached again (see the main text). (b) Picking up the second flake (MoS₂), the position of the flake is well aligned relative to the first flake. (c) Graphite-MoS₂ structure is placed on the NbSe₂ flake.

Placing the stack to the substrate

After picking up all flakes that we plan, the stack needs to be placed on a substrate where the future steps of the device fabrication will be done. In our case, NbSe₂ flakes typically has a strong bond to the substrate, and thus to avoid damaging the flake while picking up process, we put the graphite-MoS₂ heterostructure on the substrate with the NbSe₂ flake, Fig.3.6 (c). This is possible to do only for the bulk NbSe₂ flakes. We did not observe any contribution from the substrate for our devices with an average thickness of NbSe₂ around 10 nm.

To transfer a graphite-MoS₂ heterostructure onto the NbSe₂ flake, the transfer slide with the heterostructure is placed in contact with the flake at a temperature of around 80 degrees, as for the previous steps. The contact area between the PC film and the substrate is then increased by moving the slide downward and by raising the temperature to 150 degrees of the microscope stage. This increases the adhesion of the PC film to the substrate. After waiting for around 3 minutes at high temperature, the process of lifting the transfer glass can be started. As the first step, when the transfer slide is moved up, the PC film and the PDMS are separated from each other. Then, one needs to tear the PC from the transfer slide by moving the transfer slide in different directions⁶. In our project, stacking was always performed in the glove box under a microscope and using joysticks connected to the computer via Labview software.

⁶Since the PC film might be picked up together with the stack, to prevent this, we make small holes on the edges of the PC/PDMS window before placing the transfer slide in contact with the last substrate.

Removing PC film

To dissolve the PC on the stack's surface, the substrate is put in dichloromethane for one hour and rinsed in IPA. We can not use annealing to clean the surface of the stack because we have a thin flake of tunnel barrier on the top.

3.1.3 Fabrication of contacts to the stack

Here we describe the process of contacts fabrication. The fabrication process can be split into several steps; each step represents a standard process with parameters described in the Appendix7.

Since the stack is located on the substrate without markers, the first step is to draw rough markers around the stack using an e-beam lithographer. These markers will be used in the next step to create precise markers. We define these rough markers based on the distance between the stack and the edge of the substrate or between other surrounding NbSe₂ flakes and the stack. We do not metallize them at this step, as the developed pattern in the resist can be seen with the e-beam lithographer.

As the second step, we define a new precise set of markers and draw future bond places. Before depositing metal, an oxygen plasma is applied for around 20 seconds to improve the future bonding process. Metallization is done by evaporation of 5 nm of Titanium as an adhesion layer and about 60 nm of gold. Thus, we have the stack with metallized markers and bond places at this step.

Next, we analyse the stack's surface and the positions of the flakes relative to each other with the atomic force microscope. We choose the cleanest places of the stack to define tunnel contacts (in Chapter 2 we defined them as "probes"). The area of the tunnel contacts should be optimized to strike a balance between avoiding signal averaging and ensuring a large enough signal. The optimal area depends on the thickness of tunnel barrier and for 3-5 layers MoS₂ or 2 layers hBN is around $2 \mu\text{m}^2$. In the final step of fabrication, the device is electrically tested using a needle probe station, which enables the application and measurement of voltage on the device. Then, the device is mounted and mechanically attached to a chip carrier with silver glue. For the electrical connection, we bond the device with gold wires using an ultrasonic wedge bonder.

3.2 Cryogenics

Measuring QD-SC transport properties requires an electron temperature below the energy scales of the physical system, for example, the superconducting energy gap and the level spacing of the quantum dot. To reach suitable

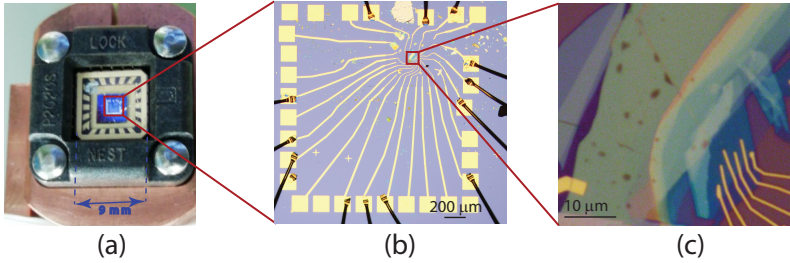


Figure 3.7 Connection of a nanoscale device to the measurement set-up. (a) The device is mounted and wire bonded to the chip carrier, and the chip carrier is loaded into the device socket of the cryostat's insert. (b) The 5x optical image of the device after bonding it to the chip carrier, the device with contact has $2 \times 2 \text{ mm}^2$ size. (c) The 100x optical image of the device. On the left, an electrode to the NbSe_2 is visible, while on the right are some of the probes/ tunnel junctions of the device.

temperatures, different types of cryostats can be used. Below we will briefly summarize only cryostats working based on liquid cryogenics.

A temperature of $\sim 4 \text{ K}$ can be reached easily by dipping the device into a vacuum-insulated vessel with liquid helium, since 4.2 K corresponds to the boiling temperature of liquid helium at 1 atmosphere. A lower temperature of $\sim 1.6 \text{ K}$ can be reached by using a cryostat, where it is possible to lower the He vapor pressure. This causes liquid helium to evaporate, releasing latent heat and cooling the liquid helium. Liquid cryogenics cryostats usually have several common components:

1. The shield structure. An outer vacuum chamber (OVC) decouples the liquid nitrogen bath from the room temperature environment. The inner vacuum chamber (IVC) separates the helium bath from the nitrogen bath. The device is located in the insert, which is a vacuum chamber surrounded by the liquid helium bath. All the devices are covered by Faraday cages that shield the device against electromagnetic fields, Fig. 3.8 (a);
2. The needle valve to allow and control helium flow into the insert or another part, for example, a "1 K" pot⁷. The pump attached to the insert evaporates incoming helium and thus cools it down below 4 K .

To achieve a temperature lower than 1 K , one can employ a ^3He cryostat. ^3He is a rare and, therefore expensive isotope of helium and at low tempera-

⁷1 K" pot is a small pumped ^4He pot, which is connected to the ^4He bath via the needle valve

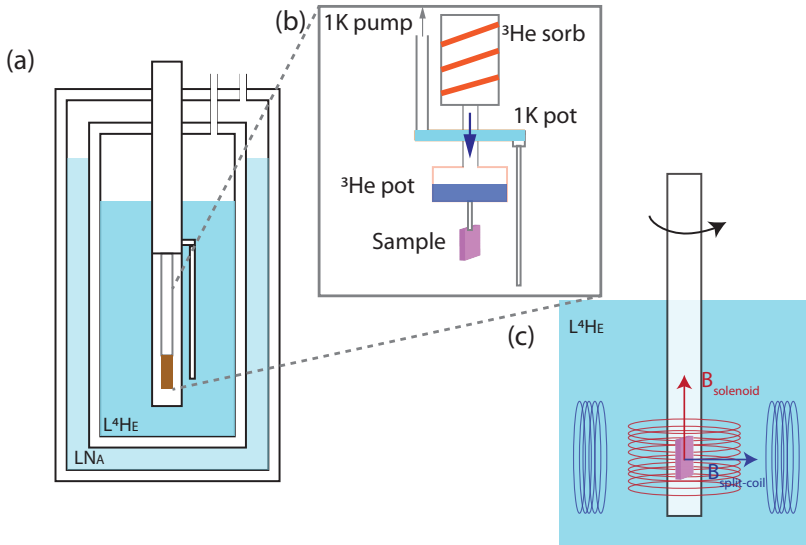


Figure 3.8 (a) Shielded structure of cryostats working based on liquid cryogenics. (b) Operation principle of a sorption pumped ^3He insert. (c) Directions of the magnetic field in the ^3He cryostat

tures, it has a much higher vapor pressure⁸ than ^4He [44]. By pumping ^3He , it is possible to reach a stable base temperature of around 260 mK in the ^3He chamber, which is in thermal contact with the device. The evaporated ^3He is collected by a charcoal sorb (^3He sorb). Releasing ^3He back from the ^3He sorb is done by heating it to around 35 K. Afterwards, the ^3He gas is cooled down and condensed by the 1 K pot ($T=1.4$ K) and the liquid ^3He collected again in the ^3He pot, Fig.3.8 (b). The temperature of $L^3\text{He}$ decreases to around 260 mK by evaporation and can be kept up to around 48 h, which is limited by the period when all ^3He evaporates from the ^3He pot. After this, the recondensation of ^3He has to be repeated to achieve the low temperature again.

Even lower temperatures, ~ 20 mK are possible to achieve with dilution cryostats. This type of cryostat employs the unusual properties of $^3\text{He}/^4\text{He}$ mixtures [44].

⁸Around 35 times higher

3.3 Measurement set-up

To study the transport properties of a sample located in the cryostat, one has to connect it with the measurement electronics, which are at room temperature. The chip carrier with the device is located in the chip socket of the cryostat's insert and connected to a break-out box, which is at room temperature. The voltage sources and read-out electronics are connected to the break-out box via BNC cables. Thus the measuring lines form a heat leak, and the sample has to be protected from the high-frequency thermal radiation (a room temperature of 25 °C corresponds to $f = T * k_B/h \approx 6 THz$).

To do so, we employ two-stage filtering. At room temperature, we use commercial LC low-pass filters (π -filters) for every source wire, which show attenuation around 40-60 dB for frequencies larger than 0.3 MHz [19]. The π -filter is attached directly to the break-out box. At low temperatures, we use a low-pass, so-called tape-worm filter[45], which was built in-house by the electronic workshop of the University of Basel. The filter consists of twenty insulated wires shielded by a metal tape⁹. The filter shows estimated attenuation of 60 dB at 1 GHz and a dc resistance of 63 Ohm[19]. The high-frequency currents are attenuated due to:

1. The skin effect created by the copper tape, which means the high-frequency currents flow close to the surface of the tape[45];
2. Capacitive coupling between wires and the grounded copper tape, which grounds the high-frequency currents;
3. A configuration of the filter as a lossy R-C transmission line, which has exponential damping with frequency.

The filter is attached directly to the cold fingers of the cryostat to anchor the measurement lines thermally.

For conductance measurement, we bias the device using DC voltage superposed with a small AC excitation and measure the current. To perform high-resolution and noise-free measurements, we use the standard lock-in techniques, where we utilize a Stanford lock-in amplifier SR830. The lock-in amplifier allows the application of an AC signal with some low-frequency¹⁰ and detects the signal only with the same frequency as the input signal. We apply an AC voltage with frequency around 78 Hz, and with a small magnitude around 10 μV to not average the measurement and degrade the energy resolution obtained by the cryostat, $eV_{AC} < k_B T$, where T is the cryostat temperature. As DC voltage source, we use a low-noise Yokogawa 7651 source.

⁹The wires are made from CuNi alloy with a core diameter of 80 μm , and the metal tape is made from copper

¹⁰The low frequency is used to minimize the capacitance

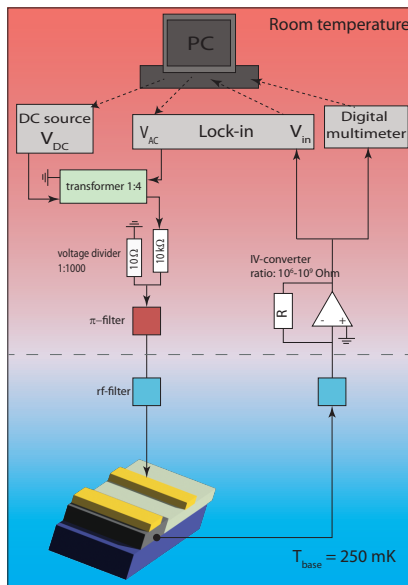


Figure 3.9 Schematic of a typical set-up for measurement of differential conductance with the lock-in technique at cryogenic temperatures. The schematic is adapted from Ref.[46]

A schematic of the measurement set-up is presented in Fig.3.9. A transformer with a 1:4 winding ratio adds the AC signal to DC voltage. The signal is further decreased 1000 times with a voltage divider, which is mounted to the break-out box before the pi-filter. After the signal passes through low-pass filters, it is applied to the probe of the tunneling device and taken out from the electrode on the sample (two-probe measurement)¹¹. Afterwards, the signal goes through a homebuilt low-noise current to voltage (I/V) converter with a conversion ratio of 10^6 - 10^9 V/A. The output signal is simultaneously measured by a digital multimeter Keithley 2000 to measure the total current and by lock-in to study differential conductance. All instruments are controlled with a computer via a General Purpose Interface Bus(GPIB) and Jupyter Notebook platform.

¹¹The signal is also possible to apply in another direction

3.4 Magnetic measurement and data processing

Other important instruments that need to be described are superconducting magnets. As shown in Fig.3.8 (c), the ^3He vertical cryostat employed for our measurements is equipped with two cryogenic magnets, which are made from Nb alloy. The solenoid magnet generates a magnetic field up to 9 Tesla (here and after in the section called B_{solenoid}) along the cryostat's axis, called the z -axis. The second magnet is a split-coil, which generates a magnetic field up to 4 Tesla (here and after in the section called $B_{\text{split-coil}}$) oriented in the horizontal x - y plane.

The sample stage of the insert allows to orient the device in any direction. In our research, we are interested in the maximum range of the in-plane magnetic field with respect to the measured heterostructure. Therefore, we orient the heterostructure along the z direction, as shown in Fig.3.10 (a). This usually leads to a slight, less than 1° , misalignment of the device plane with the direction of B_{solenoid} . It will be shown in Chapter4, that the superconducting gap of NbSe_2 is spoiled by a relatively small out of sample plane field contribution, thereby complicating attempts to study any sub-gap phenomena. Therefore it is crucial to align the magnetic field in the in-plane direction of the measured heterostructure.

The standard way to compensate for this misalignment is to use a magnetic field with perpendicular direction. Fig.3.10 (b) shows differential conductance vs. out-of device plane $B_{\text{split-coil}}$ by keeping $B_{\text{solenoid}} = 8 \text{ T}$ and $V_{\text{bias}} = 0$. Fig.3.10 (c) shows the differential conductance spectra at $B_{\text{solenoid}} = 8 \text{ T}$ and different compensation fields. The insert shows that at $B_{\text{split-coil}} \approx -550 \text{ mT}$, the conductance values is smaller than at $B_{\text{split-coil}} = -510 \text{ mT}$.

Here we presented the simplest case of the alignment at a fixed B_{solenoid} value and of a BCS-like superconducting gap. In our research, we are interested in studying sub-gap excitations in the wide range of the magnetic field. Data analysis follows the same principle as demonstrated here but is complicated for at least two reasons. First, the compensating $B_{\text{split-coil}}$ field values do not increase linearly with B_{solenoid} values as one would expect. This is most likely due to the formation of vortices in NbSe_2 , which is a type II superconductor. The second reason is that the conductance minimum is not always at $V_{\text{bias}} = 0$ due to sub-gap excitations. The whole analysis process is described in Chapter 5, after introducing the physics of such sub-gap excitations.

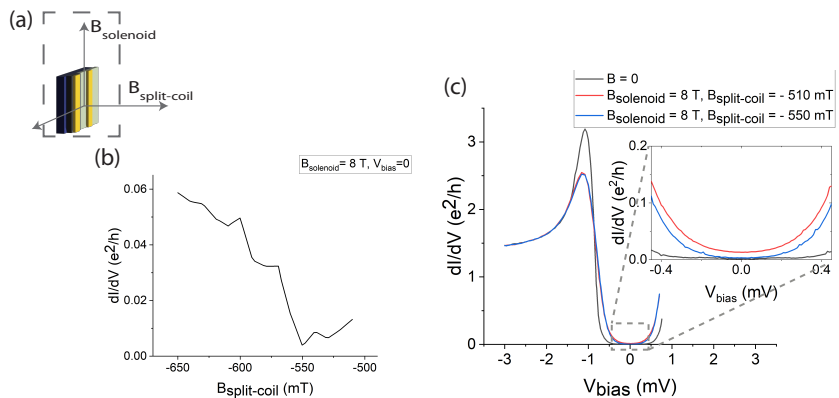


Figure 3.10 Data analysis of magnetic measurement. (a) The schematic of the sample orientation with respect to the magnetic field's axes. (b) Differential conductance as function of $B_{\text{split-coil}}$ at fixed $B_{\text{solenoid}} = 8$ T and $V_{\text{bias}} = 0$. (c) Differential conductance as a function of V_{bias} for the same tunnel junction as in (b), the black is a measurement without magnetic field, the red and blue is at $B_{\text{solenoid}} = 8$ T and different $B_{\text{split-coil}}$ compensation fields. The insert clearly shows that the in-gap conductance is less for the $B_{\text{split-coil}} = -550$ mT, compared to $B_{\text{split-coil}} = -510$ mT.

4 Characterisation of NbSe₂

As was described in chapter 2, NbSe₂ is a superconductor with unconventional properties. This chapter includes our two different experiments to characterize NbSe₂. We start with macroscopic parameter measurements of NbSe₂, such as a critical transition temperature (T_c), critical current density (j_c), and critical magnetic fields. The critical in-plane magnetic field for NbSe₂ is above the magnetic field we can apply in our laboratory. Next, we provide a fitting of NbSe₂ superconducting gap, which allows us to estimate the nature of superconductivity and the quality of our tunneling devices¹.

¹Some of the presented data was published in Ref.[27]

4.1 Characterisation of macroscopic parameters of NbSe₂ flake

The NbSe₂ bulk crystals are provided by Helmut Berger and Laszlo Forro from EPFL University. The crystals were grown by iodine vapor transport at temperatures 650-730 °C[47]. The purpose of this section is to characterize the macroscopic parameters of thin NbSe₂, for which we have fabricated a test device using a flake with a thickness of 17 nm.

4.1.1 Test device and measurement set-up

To determine the critical temperature and current of NbSe₂, we fabricated a device containing prepatterned Ti/Au contacts and placed one NbSe₂ flake with an average thickness of around 17 nm on the top. The flake from the bulk crystal was obtained by mechanical exfoliation. The fabrication details can be found in Chapter 3 and the Appendix 7. As NbSe₂ is an air-sensitive material and since we do not cover it by another flake, after gluing and bonding the device to a chip-carrier, we covered it with an e-beam resist and let it dry at room temperature. We skip the usual steps of spinning and baking the resist, to do not destroy wire-bonded connections, and to avoid increasing of the oxidation process, respectively. Fig.4.1 shows the optical image of the device. Indicated contacts were used for applying current and measuring the voltage through the device. The length of the part of the contacts, that overlaps with the NbSe₂ flake is approximately 20 μm. The distance between contacts V- and V+ is around 1.5 μm.

The measurements were done in variable temperature insert (VTI), allowing measuring in the wide temperature range from 1.6 K to 300 K. We current bias the device by applying a voltage to the large resistance of around 10 MΩ ($R \gg R_{device}$) connected in series with it. In such a way, we change DC voltage in a wide range (from -32 V to 32 V), and by adding the small AC voltage of around 0.01 V by the lock-in amplifier, we obtain low-noise dV/dI measurements.

4.1.2 Critical current density j_c and critical temperature T_c

In Fig.4.2, dV/dI is presented as a function of the bias current (I_{bias}) and the temperature. According to the data, the 17 nm flake of NbSe₂ has a critical current $I_c \approx 2$ mA at 1.64 K. Considering the device geometry, the critical current density (j_c) is approximately $5.9 \cdot 10^5$ A/cm². This magnitude is consistent with j_c presented in Ref.[48, 49]. The significant change of the critical current at the temperature around 2 K is most likely related to the lambda point of the helium, when the transition from a superfluid to the non-superfluid phase occurs, thus leading to different thermalization.

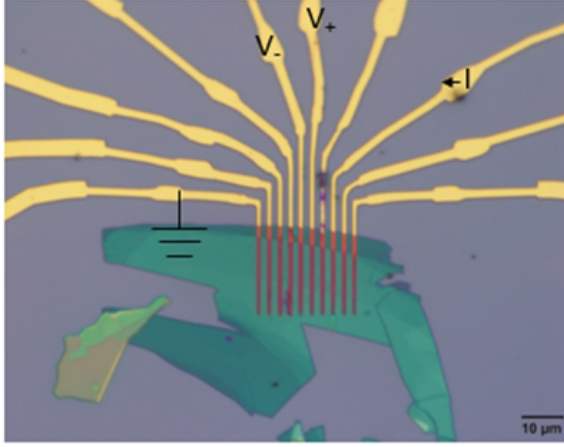


Figure 4.1 Optical image of the test device used to measure the critical current and temperature of NbSe₂. There are Ti/Au bottom contacts and a 17 nm thick NbSe₂ flake on the top. The indicated contacts were used for the data provided below. The device is covered with the e-beam PMMA resist to prevent oxidation.

According to Fig.4.2, the critical temperature (T_c) at $I_{bias} = 0$ is around 6 K. The temperature dependence of the critical current shows a parabolic behavior and is in qualitative agreement with the BCS theory, described by the following equation[7]:

$$\Delta(T \rightarrow T_c) \approx 3.06k_B T_c \sqrt{1 - \left(\frac{T}{T_c}\right)}, \quad (4.1)$$

where k_B is Boltzmann constant, and T_c is the critical temperature of superconducting state.

4.1.3 Magnetic characterisation of NbSe₂

Next, we study the behavior of NbSe₂ in perpendicular magnetic field, demonstrated in Fig.4.3. According to the data presented in this plot, the critical perpendicular magnetic field is around 3.5 T for 17 nm flake of NbSe₂ at 1.6 K and $I_{bias} = 0$. The superconducting zero-resistance region decreases significantly with the rise of the magnetic field. We believe this is due to orbital depairing since the cyclotron radius would be smaller than the lateral size of the flake.

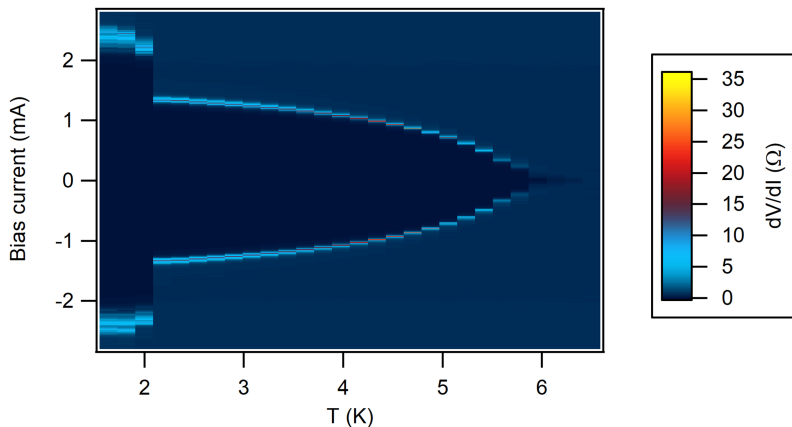


Figure 4.2 dV/dI as a function of temperature and bias current. A dark blue color indicates the superconducting region. The temperature was varied in increments of 0.2 K during the measurement.

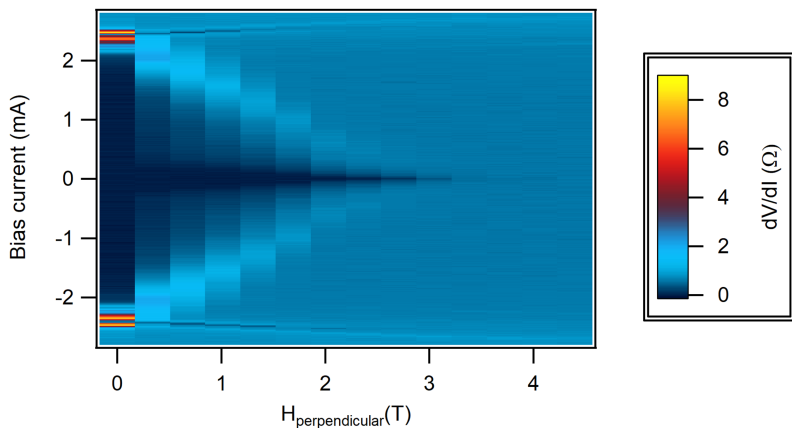


Figure 4.3 dV/dI as a function of temperature and perpendicular to the flake magnetic field. A dark blue color indicates the superconducting region. The measurement is conducted at $T=1.6$ K. The measurement from 0 to 3 T was done with a step equal to 0.5 T and from 3 to 4.5 T with a step equal to 0.2 T to determine the critical magnetic field H_{c2} accurately.

All the following measurements in this chapter are shown for tunneling devices. As was described in Chapter 2, tunneling spectroscopy allows to directly measure the density of states of the sample. The fabrication details are provided in Chapter 3 and Appendix 7. In these devices, NbSe₂ thickness is around 10 nm. The measurements were conducted at 250 mK. For this, we used the Heliox ³He cryostat and the devices were oriented such, that the maximum in-plane magnetic field is 9 T and the maximum perpendicular field is 4 T.

Fig. 4.4 depicts dI/dV as a function of bias voltage and the perpendicular magnetic field. The significant softening of the superconducting gap could be observed.

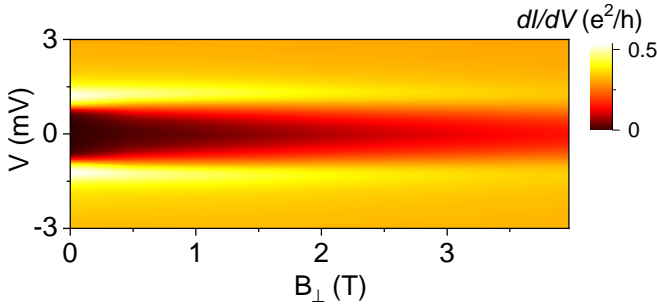


Figure 4.4 (a) dI/dV as function of the bias voltage and the perpendicular to the device plane magnetic field. The magnetic field leads to the softening of the superconducting energy gap.

Fig. 4.5 presents dI/dV as a function of bias voltage and the parallel magnetic field. It is easy to notice that compared with Fig. 4.4, the superconducting gap remains robust and almost unchangeable up to 9 T, which is limited only by the cryostat magnet. This is likely due to the absence of orbital effects, but having the intrinsic strong Ising spin-orbit coupling [17]. This makes NbSe₂ an excellent platform for studying different phenomena in high in-plane magnetic fields.

4.2 Superconducting gap of NbSe₂ and its fitting

In this section, we analyse the quality of the NbSe₂ - based tunnel junction by calculating the suppression factor and the transparency of the tunnel barriers. It is known from the literature [50] and was observed in our experiment that NbSe₂ has a superconducting gap that differs from a single isotropic gap (BCS case). Therefore, in this section, we also implement three different models to

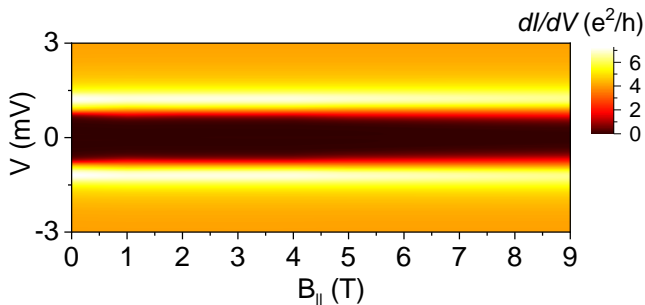


Figure 4.5 (a) dI/dV as function of the bias voltage and the parallel magnetic field. The measurement shows that the superconducting energy gap is robust to the in-plane magnetic field.

fit the NbSe₂ superconducting energy gap. Additionally, we show the fitting of the superconducting gap as a function of an in-plane magnetic field.

4.2.1 Quality of the tunnel junctions

In Fig.4.6, we present one of our NbSe₂ tunneling spectra, which shows a well-defined superconducting gap. We plot the same data in a logarithmic scale in the top panel to estimate the suppression factor: $G_N/G_0 \geq 800$, where G_0 represents the differential conductance inside the superconducting gap at zero bias and G_N represents the differential conductance outside the gap. Other tunnel junctions also typically show a high suppression factor² with $G_N/G_0 \geq 100$, demonstrating the high quality of the tunnel junctions and suppression of quasiparticle transport.

Furthermore, we use the Sharvin's expression to estimate the transparency of our tunneling barriers[50], [51], [52]:

$$G_N = \frac{2e^2}{h} \frac{k_F^2 A}{4\pi} \mathcal{T},$$

where G_N is the differential conductance outside of the superconducting gap, A is the lateral area of the junction, k_F is the Fermi momentum and \mathcal{T} is the average transmission of the conductance channels[50].

Normal conductance for the considered tunnel junction is $G_N = 0.3 e^2/h$ and $A=1.56 \mu\text{m}^2$. In NbSe₂ $k_F \sim 5 \times 10^9 \text{ m}^{-1}$ [50]. Therefore, we have $\mathcal{T} \sim 5 \times 10^{-14}$. Tunnel barriers with such low transparency are well suited for tunneling experiments.

²See the table of all tunnel junctions in Chapter5

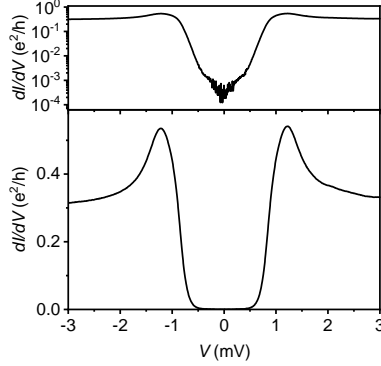


Figure 4.6 dI/dV as function of bias voltage. The dependence shows the superconducting gap with the suppression factor $G_N/G_0 \gtrsim 800$.

4.2.2 Fitting of the superconducting energy gap

The fitting was done with Mathematica software. We mainly used data measured from the device consisting of 10 nm thick NbSe₂ flake, MoS₂ flake as a tunnel barrier, and Ti/Au normal leads. We fixed the temperature $T = 255$ mK for all fits provided here, which corresponds to the measurement temperature.

As was discussed in Chapter 2, the density of states is proportional to differential tunneling conductance. For the tunneling conductance G_{NS} we use the standard equation[53]:

$$G_{NS} = dI/dV = \frac{G_{NN}}{N_N(0)} \int_{-\infty}^{+\infty} N_S(E, \Gamma, \Delta) \frac{df(E + eVb, T)}{d(eVb)} dE \quad (4.2)$$

where G_{NN} is the tunneling conductance when both electrodes (Ti/Au and NbSe₂) are in the normal state; $N_N(0)$ and N_S are the density of states at the Fermi level for the superconducting electrode in the normal and superconducting state, respectively; $f(E+eVb)$ is the Fermi-Dirac distribution[53]. Here we assume that the thermal broadening is much less than the superconducting gap; thus, there is no quasiparticle inside the superconducting gap.

In Fig.4.6, it is possible to see that the superconducting gap deviates from the BCS-like superconducting gap (an isotropic, single gap). Furthermore, it is well known in the literature that NbSe₂ superconductivity is unconventional, and superconducting gap presents either a single anisotropic gap or a two-band gap[54]. We considered the anisotropy model and the two-band model

and compared the result with the BCS model to clarify using our experimental results, which one is the most probable reason for superconductivity in NbSe₂.

For the anisotropy model, the superconducting gap is described as function of the anisotropy parameter (A) and polar angle (θ) of hexagonal plane[53]. Angle (θ) denotes the angle between relative to the center of mass coordinate of the Cooper and a axis in the hexagonal plane[55]. By accounting also that the Fermi surface of NbSe₂ has six-fold symmetry around Γ point, the equation for superconducting gap can be written as[53]:

$$\Delta(\theta, A) = \Delta_0[A \cdot \cos(6\theta) + (1 - A)], \quad (4.3)$$

where Δ_0 is the maximum value of the superconducting gap.

To find the average value of N_S we use integrated Dynes equation for the DOS [53], divided by the interval of integration:

$$N_S(E, \Gamma, \Delta, A) = \text{Re} \left\{ \frac{1}{2\pi} \int_0^{2\pi} \frac{E - i\Gamma}{\sqrt{(E - i\Gamma)^2 - \Delta(\theta, A)^2}} d\theta \right\} \quad (4.4)$$

where Γ is a Dynes broadening parameter, Δ is a superconducting gap, A is an anisotropy parameter of superconducting gap.

Another important case to consider is the two-band model, since it was shown by angle-resolved photoemission spectroscopy and density functional theory calculation that the Fermi energy in NbSe₂ is crossed by five independent electronic bands[56],[57]. Four are Nb-derived bands, and one is from Se p_z orbitals. The Nb-derived bands have different DOS and electron-phonon coupling than the Se-derived band. In the literature, this is described by the two-band model [50]. The superconducting DOS can be written as a sum of DOS for the first type band and the second type band as following[53]:

$$N_S(E, \Gamma_1, \Delta_1, \Gamma_2, \Delta_2) = \text{Re} \left\{ C \frac{E - i\Gamma_1}{\sqrt{(E - i\Gamma_1)^2 - \Delta_1^2}} + (1 - C) \frac{E - i\Gamma_2}{\sqrt{(E - i\Gamma_2)^2 - \Delta_2^2}} \right\}, \quad (4.5)$$

where Δ_1, Δ_2 are the two values of superconducting gaps, Γ_1, Γ_2 are quasi-particle lifetime broadening, and C represents the contribution from the different pockets of the Fermi surface.

Results for all three models are presented in Fig.4.7. To recover the BCS model from the anisotropy model, we set the anisotropy parameter to zero. The two-band model provides the best fitting for NbSe₂ with a thickness of around 10 nm. For monolayer NbSe₂ and very thin flakes, the superconducting gap is described by a single gap model according to the band structure calculations[50].

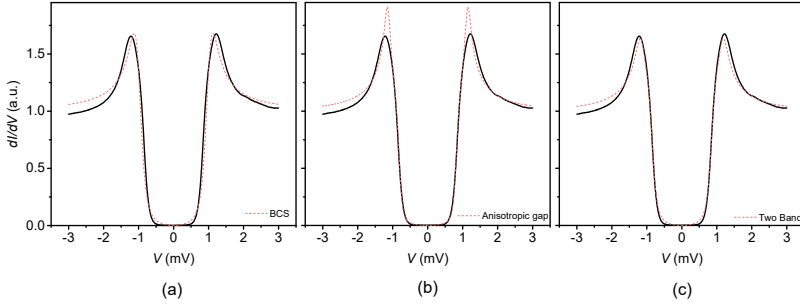


Figure 4.7 Tunnel spectra fitting. (a) A single gap BCS model with parameters $\Delta = 1.0$ meV, $\Gamma = 0.11$ meV. (b) A single anisotropic gap with $\Delta = 1.14$ meV, $\Gamma = 0.045$ meV and $A = 0.15$. (c) Two band model with parameters $\Delta_1 = 1.1$ meV, $\Gamma_1 = 0.08$ meV, $\Delta_2 = 0.9$ meV, $\Gamma_2 = 0.08$ meV.

Fitting of the superconducting gap under in-plane magnetic field

In this section, we investigate the superconducting gap as a function of an in-plane magnetic field. The results of the fitting for the two different tunnel junctions are presented in Fig.4.8. The tunnel junction no.10 (red) represents the same tunnel junction which was measured in Fig.4.5. The fit shows, that the superconducting gap values remain constant. The fluctuation of gap values around two percent, we attribute to not ideal fitting by the anisotropy model. The experimental results and the fitting suggest that the superconducting energy gap does not change under the in-plane magnetic field up to 9 T. Similar trends are observed in other tunnel junctions with around the same thickness of NbSe₂.

We connect the above mentioned robustness of the superconducting gap with the absence of orbital effects and presence of strong intrinsic spin-orbit coupling. Monolayer NbSe₂ has a strong spin-orbit coupling as a result of its broken inversion symmetry and the presence of the 4d element (Niobium). In our case of few-layers NbSe₂, the crystal also exhibits spin-orbit coupling, even when the inversion symmetry is restored. This happens due to weak van der Waals bonding between layers, as was shown in Chapter 2. In materials without spin-orbit coupling, the upper critical in-plane magnetic field (H_{c2}), is equal to the Pauli limit ($H_p = 1.86T_c$), as discussed in Chapter 2. Therefore, for a 10 nm NbSe₂ with $T_c < 6$ K, the Pauli limit is less than 11 T. In our lab, we can apply a magnetic field only up to 9 T. Still, from the obtained experimental data and the presented fitting, it is likely that H_{c2} will be higher than the Pauli limit.

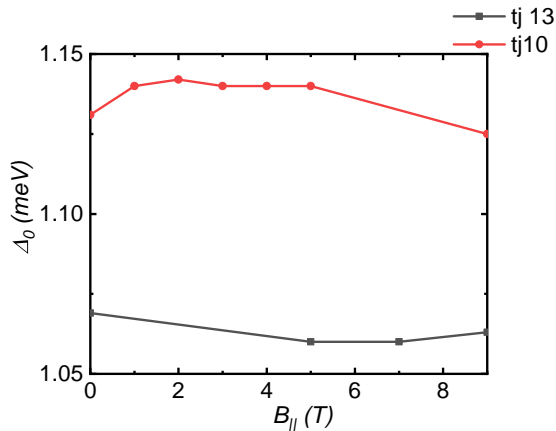


Figure 4.8 Fitting of the superconducting gap as a function of the in-plane magnetic field. The data is provided for two different tunnel junctions. The superconducting gap remains relatively constant with slight fluctuations of less than two percent. This indicates that the superconducting gap remains unchanged under an in-plane magnetic field up to 9 T. The anisotropy model is used to fit this data.

Additionally, we observed an increase of the broadening and anisotropy parameters with an in-plane magnetic field, as shown in Fig.4.9. While the Dynes parameter Γ might increase due to warming the device by the applied magnetic field or different types of scattering [58], a change in anisotropy might be due to the effect of the magnetic field on the crystal symmetry

4.3 Summary

In this chapter, we presented our experimental data and its analysis, proving that NbSe₂ has robust superconductivity even for relatively thin flakes with a thickness in the order of 10 nm. The relatively high critical temperature, around 6 K, and the robustness to the in-plane magnetic field, make NbSe₂ the perfect platform to investigate the phenomena in the high magnetic field. Next, we analyzed the quality of van der Waals NbSe₂-MoS₂ tunnel junctions. NbSe₂ shows a very well-defined superconducting gap with suppression factors higher than 100. Additionally, we showed that the transparency of the tunnel barrier has a very small value. Both these characteristics show that we have high-quality tunnel junctions. Furthermore, it was noticed that the NbSe₂

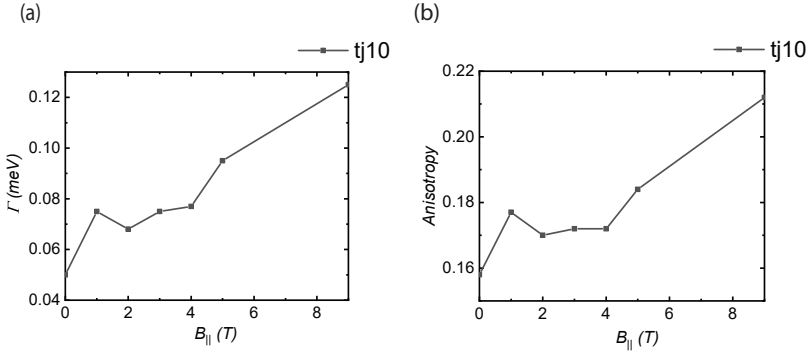


Figure 4.9 Dynes' broadening parameter (a) and the anisotropy parameter (b) versus the in-plane magnetic field for tunnel junction no.10 of the device "D21". This tunnel junction and others show an increase in these parameters with the in-plane magnetic field. While the broadening parameter might increase due to the device's warming up under a magnetic field or different scattering mechanisms, a reason for anisotropy's increase is not evident.

energy gap deviates from the single isotropic energy gap given by BCS theory. We provided the fitting for our experimental data, proving that the two-band model gives the best fitting for the NbSe₂ with a thickness of around 10 nm. As the last step, we proved by fitting that the superconducting energy gap of NbSe₂ remains constant, suggesting that the upper critical magnetic field is larger than the Pauli limit. The most probable reason for it is the large spin-orbit coupling in NbSe₂, which makes this material promising for observing topological superconductivity [59].

5 Subgap states in NbSe₂-MoS₂ heterostructures

Superconductivity in van der Waals materials, such as NbSe₂ and TaS₂, is fundamentally novel due to the effects of dimensionality, crystal symmetries, and strong spin-orbit coupling. In this work we perform tunnel spectroscopy on NbSe₂ by utilizing MoS₂ or hexagonal Boron Nitride (hBN) as a tunnel barrier. We observe subgap excitations and probe their origin by studying various heterostructure designs. We show that the edge of NbSe₂ hosts many defect states, which strongly couple to the superconductor and form Andreev bound states. Furthermore, by isolating the NbSe₂ edge we show that the subgap states are ubiquitous in MoS₂ tunnel barriers, but absent in hBN tunnel barriers, suggesting defects in MoS₂ as their origin. Their magnetic nature reveals a singlet or a doublet type ground state and based on nearly vanishing g-factors or avoided-crossing of subgap excitations we highlight the role of strong spin-orbit coupling¹.

¹Parts of this chapter were published in a similar form in Ref.[27]

5.1 Introduction

Superconductivity in the two-dimensional limit is driven by a unique interplay between dimensionality, crystal symmetries, correlated electron effects and, if present, the role of spin-orbit coupling. This often results in various competing ground states and gives rise to rich novel phenomena. Ultimately two-dimensional van der Waals superconductors are illustrative examples. Naturally superconducting NbSe₂ and TaS₂ have been recently isolated and studied [17, 30], and MoS₂ has been doped into a superconducting state [60]. In their monolayer or few-layer forms these van der Waals superconductors display novel phenomena, such as the survival of superconductivity up to tens of Teslas of applied in-plane magnetic field [17, 30], layer dependent superconducting properties [17] and competition with other phases [61]. Furthermore, it is predicted that these materials can be externally tuned to host novel topological phases [59, 62] and there are expectations of the presence of unconventional pairing mechanisms in Ising superconductors [31].

These features essentially result from the large spin-orbit coupling (SOC) and the crystal symmetry in these materials. For this SOC, called the Ising-type, the corresponding spin orbit magnetic field points out-of-plane and in opposite directions in the opposite valleys of the hexagonal Brillouin zone of these materials [30, 60]. This splits the spin degenerate bands and the majority singlet Cooper pairs are expected to be formed from opposite valleys. As the large spin orbit magnetic field (some estimates indicate $B_{so} \sim 100$ T [60]) pins the spins out-of-plane, an applied in-plane magnetic field (usually smaller than B_{so}) hardly affects the electron spins and thus the Cooper pairs survive large Zeeman fields.

Recently, proximity induced superconductivity in semiconducting nanostructures has been widely investigated [8, 23, 63–65], primarily driven by the proposals for topological quantum computation [66, 67]. Additionally, low dimensional structures coupled to van der Waals superconductors with large SOC provide a rich platform to investigate the nature of Andreev bound states. It may also offer insights into the unconventional superconducting properties. In this regard, tunnel spectroscopy is a versatile tool to probe the superconducting density of states (DOS). Electronically gapped van der Waals materials provide high quality tunnel barriers that allow an unprecedented control over the barrier thickness and the interface quality. They are also especially well suited to probe the air-sensitive van der Waals superconductors [53, 68]. Tunnel spectroscopy in such heterostructures has revealed the presence of Andreev levels in the subgap spectrum [68, 69]. However, the exact origin and nature of these bound states has not been systematically investigated, and it is not known if such bound states reside in the tunnel barriers or are hosted on the NbSe₂ surface [70–72]. The role of spin-orbit coupling in determining the Andreev level ground state and their magnetic nature also remains to be

understood.

5.2 Results and discussion

In this work we perform tunneling spectroscopy on NbSe₂ by utilizing MoS₂ or hexagonal Boron Nitride (hBN) [73] as a tunnel barrier and Ti/Au as the normal leads. We find that the single particle gapped spectrum is often interrupted by the presence of subgap excitations and we probe their origin by studying various heterostructure designs. We show that the edge of NbSe₂ hosts many defect states, some of which are strongly coupled to the superconductor. However, we also observe subgap excitations in devices where the NbSe₂ edge is electrically isolated. We show that these subgap excitations arise from defects in MoS₂ and are absent in hBN tunnel barriers. We probe the magnetic nature of these subgap states by studying their evolution in applied magnetic fields and reveal the nature of ground states, as well as highlight the role of spin-orbit coupling.

The normal-insulator-superconductor (NIS) type planar tunnel junctions are fabricated by stacking MoS₂ (3–5 layers) or hBN (3 layers) on NbSe₂ crystals (~ 3 nm – 20 nm) in a glovebox in N₂ atmosphere. MoS₂ or hBN act as the tunnel barrier and prevent NbSe₂ from oxidation. We have studied 8 devices and over 50 tunnel junctions and a summary of results is presented here. In Chapter 3, one can find future information regarding the fabrication of the devices. We present the device parameters in summary table in the end of this chapter.

Unlike the spectrum shown in Chapter 4, however, we often observe discrete subgap features in MoS₂ tunnel barrier junctions, see Fig.5.1a. Such subgap features can result from discrete electronic states in the tunnel path, modified by the superconducting proximity effect. The discrete states themselves may arise from a defect or an impurity in the tunnel barrier or on the surface of the superconductor [70–72]. The formation of such Andreev levels has recently been widely explored, especially in semiconducting nanowires coupled to superconductors, and is fairly well understood [8, 23, 65]. We model the defect state as a quantum dot coupled to a superconductor, in a similar way as was describe in Chapter 2. In this work, we discuss the subgap features in terms of the Andreev bound states and this framework holds when the quasiparticles in the superconductor do not play a role. However, in principle our experiments cannot distinguish if the singlet is the superposition of $|\uparrow\rangle$ and $|\downarrow\rangle$ (Andreev bound state) or is formed between one electron on the dot and another on the superconductor (Yu-Shiba-Rushinov state) [74–76]. Quasiparticles in the superconductor could play a role if $\Delta \sim \Gamma_s$.

Applying a dc voltage bias V across the tunnel barrier, that is equivalent to the energy of the excited state, results in the transfer of a single electron

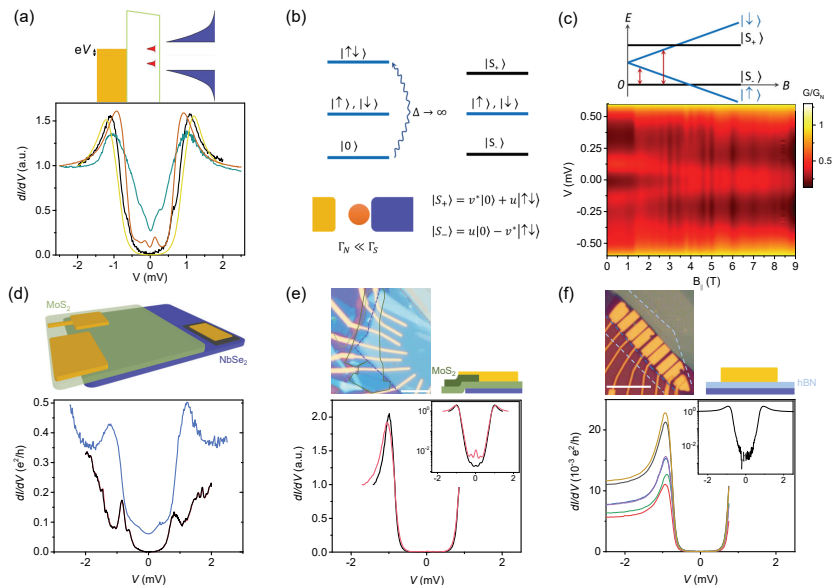


Figure 5.1 Origin of subgap states. (a) dI/dV measurements show the presence of subgap excitations. Schematic shows a possible mechanism where a defect strongly couples to the superconductor. Normalised dI/dV is shown for four different junctions in device D10. (b) The electronic states in a quantum dot are modified when it is strongly coupled to the superconductor. (c) Magnetic field evolution of the subgap excitations indicates that at $B = 0$ the ground state is a singlet but the system undergoes a quantum phase transition to a doublet ground state at a finite magnetic field. Red arrows denote the excitation energies in the schematic. The jumps in magnetic field are a result of imperfect alignment of the B_{\parallel} that leads to discrete units of flux entering the tunnel junction area. (d) dI/dV measurements on the edge of NbSe₂. Repeated runs are shown by black and red lines (barely visible, lie on top of each other), while another edge contact is shown in blue. (e) dI/dV measurements with the edge of NbSe₂ electrically isolated by using a thicker MoS₂ (solid green outline) at the edge of NbSe₂ (blue dashed line). Scale bar is 5 μm . Inset in a log-scale highlights the presence of subgap excitations. (f) dI/dV measurements for hBN used as a tunnel barrier, shows absence of subgap excitations. Inset in log-scale shows the absence of subgap excitation down to the measurement noise floor. Scale bar in the optical image is 10 μm .

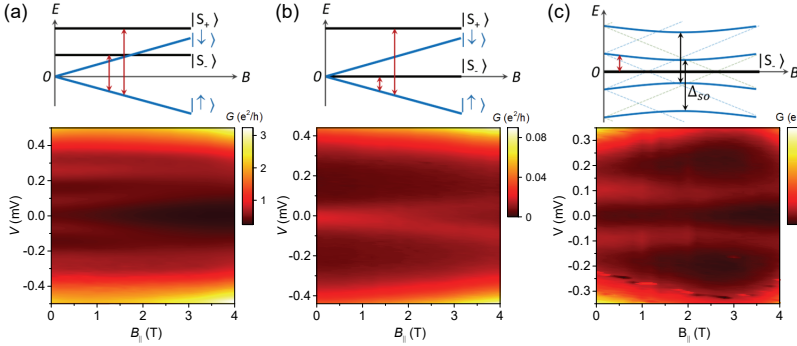


Figure 5.2 Anomalous subgap excitations. (a) Multiple subgap states are seen at $B = 0$, they evolve with an applied in-plane magnetic field but with a different g-factor. (b) dI/dV measurements show a zero bias excitation at $B = 0$, which splits in magnetic field. The transition to the higher singlet is likely at the gap edge and is not visible in our measurement. (c) Subgap excitations show an avoided crossing feature with a minimal splitting of ≈ 0.185 meV at $B_{||} \approx 2$ T.

into the dot (with N electrons) from the normal lead. This electron can form a Cooper pair to enter the superconductor and consequently a hole is retro-reflected into the normal lead. Symmetric across the Fermi energy a time-reversed process occurs and can be observed as a similar feature at the opposite dc voltage bias. Thus, the electron-hole symmetric subgap features in tunnel spectroscopy probe the excitation energy of the subgap states (N to $N \pm 1$ transitions). An external magnetic field causes Zeeman splitting of the spin degenerate doublet states and provides a key tool to study the nature of the localised ground states, see Fig.5.1c and the discussion later.

We first investigate the origin of such subgap excitations - whether they reside in the tunnel barrier or on the surface of the superconductor [70–72]. We notice that the tunnel junctions with a large overlap with the edge of the NbSe₂ crystal exhibit multiple features in dI/dV both outside and inside the gap, see Fig.5.1d. The repeatability of these features in multiple sweeps indicates that they represent discrete energy levels and do not arise from time dependent noise. They likely arise from defects present at the NbSe₂ edge cleaved during exfoliation, some of which strongly couple to the superconductor and show up as subgap excitations. The features outside the gap may be understood as resonant features arising in the normal-dot-normal system. While it may not be surprising that the NbSe₂ edge hosts many defects, this may be critical for the topological edge states predicted in NbSe₂ with an applied in-plane

magnetic field [59, 62]. Instead, it would be crucial to engineer the boundary of the topological and the trivial phase on the bulk of NbSe₂, as in a recent study [77].

In a simple planar tunnel junction a part of the normal 'wire' always crosses the NbSe₂ edge, see Fig.5.1d schematic. Therefore, next we address the question - if all the subgap states that we observe arise from such defect states at the edge of NbSe₂. We do this by electrically isolating the NbSe₂ edge by transferring additional MoS₂ layers over the edge of NbSe₂, see the optical image and the schematic of Fig.5.1e. The corresponding dI/dV curves plotted in Fig.5.1e exhibit a well-behaved superconducting gap. The subgap states are now rare, but still present in multiple junctions, as shown in the inset. This points to other source(s) of defect states, in addition to those at the edge of the NbSe₂ crystal. The possibilities that remain are the defect states in the tunnel barrier or on the surface of the superconductor.

To address this, we replace the MoS₂ tunnel barrier with 3 layers of hBN, known to be an effective tunnel barrier. In particular, the defect density in hBN is small [73, 78] and likely three orders of magnitude smaller than that in MoS₂ [79–82], although we are not aware of direct comparative studies. The differential conductance for six such tunnel junctions, each with an area $\sim 10 \mu\text{m}^2$, is shown in Fig.5.1f. While tunnel spectroscopy shows a well behaved superconducting gap with a suppression factor $G_N/G_0 \sim 300$, we do not observe subgap features in any hBN tunnel junction down to our measurement resolution, as evident from the log-scale plot in the inset of Fig.5.1f. This leads us to believe that the subgap features in MoS₂ / NbSe₂ tunnel junctions arise either from the edge of the NbSe₂ crystal or defects in MoS₂ that strongly couple to the superconductor.

Further, we study the subgap excitation spectrum in an applied in-plane magnetic field. The Zeeman splitting of the doublet states $\{|\uparrow\rangle, |\downarrow\rangle\}$ results in unique features in the excitation spectrum which allows the identification of the ground state. One such measurement is shown in Fig.5.1c, where at $B_{\parallel} = 0$ two subgap excitations are visible at $V \approx \pm 0.13$ mV. With an applied in-plane magnetic field B_{\parallel} the subgap features split (effective g-factor of ~ 0.7), where one branch moves towards zero bias and the other (weakly visible for $V > 0$) moves towards the gap edge (see SI for the second derivative). The overall behavior can be understood by considering that the dot is in a singlet $|S_{-}\rangle$ ground state at $B_{\parallel} = 0$. At $V \approx 0.13$ mV, the chemical potential of the normal lead is aligned to the spin degenerate doublet excited state. With increasing B_{\parallel} , the doublet splits resulting in the excitation energy to the lower branch decreasing while the excitation energy to the upper branch increases, as illustrated in the Fig.5.1c schematic. In fact, for $B_{\parallel} > 6$ T when the lower branch crosses zero energy, the system undergoes a quantum phase transition and the ground state changes to the doublet ground state. See SI for another such example. The appearance that the bound state sticks to zero energy

for $B_{\parallel} > 6$ T, is either the result of two wide ($FWHM \sim 0.18$ meV) bound states crossing or the influence of spin-orbit mixing with higher orbital levels, as discussed later.

The ground state of the dot coupled to a superconductor depends on the relative strengths of various energy scales - the tunnel coupling of the dot to the superconductor Γ_s , the charging energy U , the superconducting gap Δ , and the energy of the dot level relative to the chemical potential of the superconductor ξ_d . Since a finite Γ_s is necessary for the visibility of the subgap excitations and a large Γ_s favors a singlet ground state, we observe singlet states nearly six times as frequently as doublet ground states (see SI for a count of ground states). One such case is shown in Fig.5.2a, where the excitations at $\approx \pm 0.08$ meV ($B_{\parallel} = 0$) move to higher absolute energies with an applied B_{\parallel} , expected for a doublet ground state. The schematic in Fig.5.2a demonstrates the mechanism. The subgap excitation visible at higher energies $\approx \pm 0.25$ meV ($B_{\parallel} = 0$) may be attributed to the transition to the higher singlet. But this is unlikely due to a different g-factor. Instead, this may result from another parallel Andreev bound state formed via a second defect, in a junction of size $\approx 3.5 \mu\text{m}^2$, and large SOC may result in a nearly vanishing g-factor as discussed later. Rarely, a zero-bias peak is also observed at $B_{\parallel} = 0$ and we believe this results from an accidental degeneracy of the doublet and the lower singlet $|S_{-}\rangle$. One such spectrum along with the excitation energy schematic is shown in Fig.5.2b, where a zero-bias peak is observed for $B_{\parallel} = 0$ and splits for finite B_{\parallel} .

Finally, an avoided-crossing like feature, is shown in Fig.5.2c where the subgap excitations move towards zero bias but at $B_{\parallel} \approx 2$ T they start to move to higher absolute energies. We attribute this to the spin mixing and hybridisation of the doublet states that arise from higher orbital levels, due to SOC in the host material [83], as illustrated in Fig.5.2c schematic. The size of the splitting depends on the details of the defect which determine the strength of SOC and the relative directions of B_{SO} and B_{\parallel} . No hybridisation occurs when the externally applied magnetic field is parallel to the internal spin orbit field [84, 85]. This may explain why splitting is not observed in other junctions. A large spin-orbit gap (compared to the doublet excitation energy), would also result in a reduced effective g-factor (see also Fig.5.2a).

5.3 Conclusion

In conclusion, we have performed tunnel spectroscopy on NbSe₂ by utilizing MoS₂ or hexagonal Boron Nitride (hBN) as a tunnel barrier and Ti/Au as the normal leads. We find that the single particle gapped spectrum often exhibits the presence of subgap excitations and we probe their origin by studying various heterostructure designs. We show that the edge of NbSe₂ hosts many

defect states, some of which are strongly coupled to the superconductor. However, we also observe subgap excitations in devices where the NbSe₂ edge is electrically isolated. We show that while the subgap excitations are fairly ubiquitous in MoS₂ tunnel barriers they are absent in hBN tunnel barriers, suggesting that these subgap excitations arise from the defects in MoS₂. The evolution of subgap excitations in an applied in-plane magnetic fields allows us to probe the magnetic nature of the participating subgap states and reveals the nature of subgap ground states. Subgap excitations that anti-cross or show no dispersion with the Zeeman field highlight the role of spin-orbit coupling in the system.

5.4 Supporting information

In this section, we show two more examples of ground-state transitions. Additionally, we consider the thermal broadening effect on the excitations that we presented before. Next, we present the table of all devices measured for this project with their parameters, where we focus on the ground state type and summarise this with a bar chart. As the last step, we described the data analysis of magnetic measurements for tunnel junctions with the sub-gap excitations.

5.4.1 Additional subgap spectres

In Fig.5.3 and Fig.5.4, we show magnetic field evolution for another two tunnel junctions, where it is possible to observe the ground states transition from the singlet to the doublet through crossing excitations.

5.4.2 Temperature dependence of the tunnel spectra

Here we highlight the role of superconductivity by showing temperature dependent tunnel spectra. The tunnel spectra exhibits broadening with temperature, as shown in the differential conductance map in Figure 5.5a. The superconducting gap is no longer visible for $T \geq 4.4$ K and is reasonable for a thin (~ 3 nm) NbSe₂. In addition, the subgap excitations visible at a base temperature $T = 270$ mK are no longer visible at $T = 1.5$ K, as shown in Figure 5.5b. Similarly, for another device D21, shown in Figure 5.5c, the subgap excitations are no longer visible at a larger temperature $T = 4$ K, and the tunnel spectrum exhibits thermal broadening.

5.4.3 Device details

The table in this section lists the details of all measured tunnel junctions, particularly geometrical parameters and the suppression factor of the super-

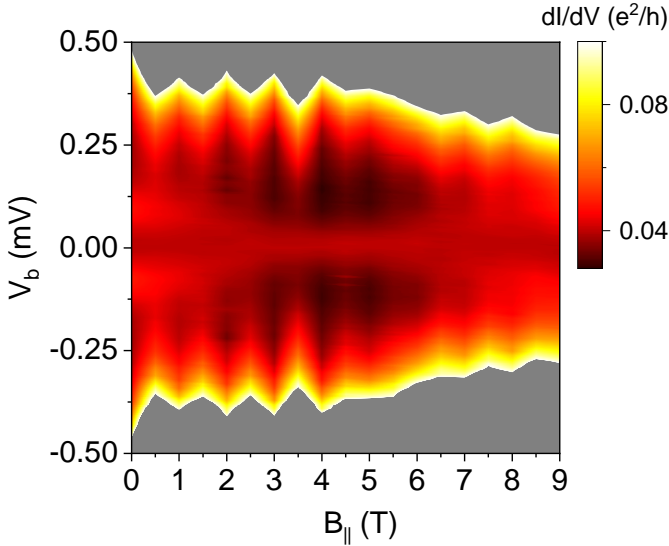


Figure 5.3 Colour map of dI/dV as a function of in-plane magnetic field B_{\parallel} and bias voltage V_b . This is another example of the transition of the ground state from singlet to doublet under in-plane magnetic field measured for the device D21, tunnel junction no.10.

conducting gap G_N/G_0 . In the column "Figure", we indicated in what figures the junction was presented. The main focus is on the type of ground state and its evolution under an in-plane magnetic field (g-factor).

The cases of the singlet ground state, a doublet ground state and accidental degeneracy are shown in the main text in Fig.5.1c, Fig.5.2a and Fig.5.2b respectively. The tunnel junctions for which either the magnetic dependence of the subgap excitations was not studied or the ground state is ambiguous, as in Figure5.6a have been categorised as 'Unknown' (ground state). The tunnel junctions for which subgap excitations were not visible, as in Figure5.6b have been categorised as 'None'.

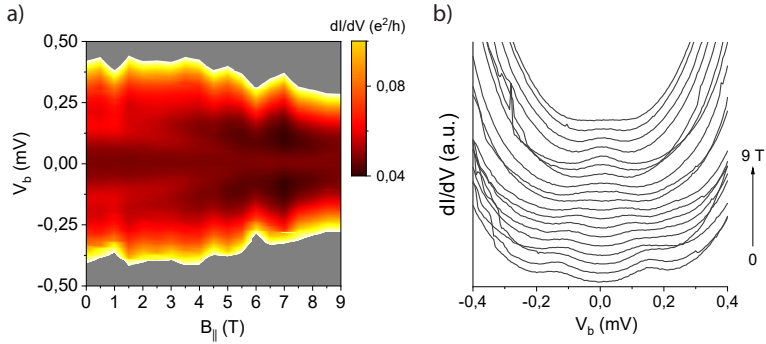


Figure 5.4 Magnetic field evolution of the subgap excitations, device D21, tunnel junction no.13. (a) Colour map of dI/dV as a function of in-plane magnetic field B_{\parallel} and bias voltage V_b . (b) Shifted differential conductance curves for the same tunnel junction as in (a). The magnetic field step size of the curves is 0.5 T. At $B_{\parallel} = 9$ T, the full width at half maximum (FWHM) is around 0.5 meV. Such a wide peak hinders us to distinguish if the lines cross as in Figure 5.3 or if the dI/dV peak sticks to $V_b=0$ above 6 T.

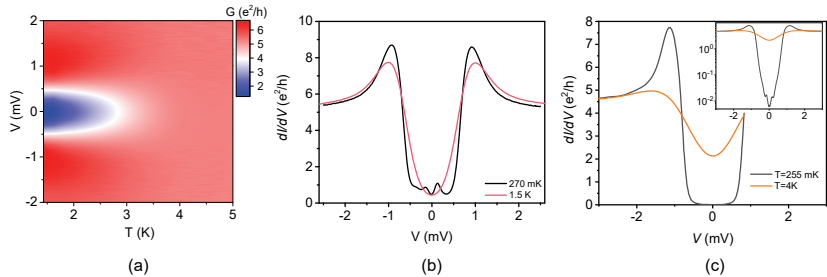


Figure 5.5 Temperature dependence of the tunnel spectra. (a) Differential conductance for device D10 as a function of voltage bias V and temperature T , starting at $T = 1.43$ K. The device has 3 nm thin NbSe₂, that's why the critical temperature is much lower than presented in Chapter 4. (b) Differential conductance measurements for device D10 show that the thermal broadening at $T = 1.5$ K is large enough that the subgap excitations are not visible when compared to $T = 270$ mK. (c) Differential conductance measurements for device D21 at $T = 270$ mK and $T = 4$ K.

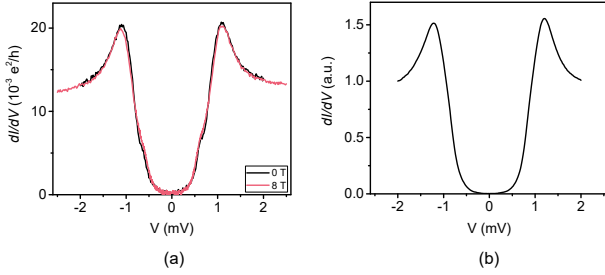


Figure 5.6 Additional definitions for the subgap ground state categories. (a) Tunnel spectra when the subgap ground state cannot be determined are categorised as 'Unknown'. Shown is an example of the subgap features that have a vanishing g-factor for junction 15 device D10. (b) Tunnel spectra where the subgap features are not visible are categorised as 'None' for junction 17 device D10.

60 Details of all measured tunnel junctions (53 junctions)									
Device	Junction	NbSe ₂ thickness, nm	Tunnel barrier, layers (L)	Area of T _j , um ²	G _N /G ₀	Ground state	g-factor	Comments	Figure (*in Ref.[27])
D10	10	3	3L MoS ₂	3.2	11	Singlet	0.70		2a, 2c, S3
	15	3	4L MoS ₂	1.1	49	Unknown	0.00	Subgap states at the gap edge	2a, S6(a)
	16	7	2L MoS ₂	2.6	4	Singlet	0.70	Approximate g factor	2a
	17	7	4L MoS ₂	2.7	400	None			2a, S6(b)
D14	1	12	4L MoS ₂	4	63	Unknown		on NbSe ₂ edge	
	5	12	4L MoS ₂	2.4	328	Singlet	0.80	Anticrossing like feature	3c
	7	12	4L MoS ₂	3.5	100	Doublet	0.64	Higher excitation has a vanishing g-factor	3a
	14	5	3L MoS ₂	1.3	1	Unknown		On NbSe ₂ edge	
	15	10	3L MoS ₂	2.3	24	Unknown			
	16	10	3L MoS ₂	2.4	4	Unknown			
	17	10	3L MoS ₂	4.1	3	Accidental degeneracy	1.70		
	18	10	3L MoS ₂	4.2	4	Unknown	0.00		
	19	10	3L MoS ₂	1.3	44	Unknown			
D19	3	7	3L hBN	10	826	None			2f black
	5	7	3L hBN	9.8	807	None			2f red
	7	7	3L hBN	10	1563	None			2f blue
	10	7	3L hBN	10	571	None			2f green
	11	7	3L hBN	10	760	None			2f violet
	16	7	3L hBN	12.2	500	None			2f yellow

Details of all measured tunnel junctions (53 junctions)									
Device	Junction	NbSe ₂ thickness, nm	Tunnel barrier, layers (L)	Area of T _j um ²	G _N /G ₀	Ground state	g-factor	Comments	Figure (*in Ref.[27])
D20	1	20	3L MoS ₂	2.7	300	Unknown		NbSe ₂ edge isolated by MoS ₂	
	2	20	3L MoS ₂	2.7	150	Unknown		NbSe ₂ edge isolated by MoS ₂	2e black
	3	20	3L MoS ₂	2.3	167	Unknown		NbSe ₂ edge isolated by MoS ₂	
	4	20	3L MoS ₂	2.5	80	Accidental degeneracy	0.55	NbSe ₂ edge isolated by MoS ₂	2e red
	5	20	3L MoS ₂	2.3	10	None			
	6	20	3L MoS ₂	3.1	27	Singlet	0.45	Doublet upper branch not visible	
D21	7	20	3L MoS ₂	3	242	None			
	8	20	3L MoS ₂	2.9	80	None			
	9	10	3L MoS ₂	1.8	131	None			
	10	10	3L MoS ₂	1.8	410	None			
	11	10	3L MoS ₂	3.2	141	None			
	12	10	3L MoS ₂	1.8	8	None			
	13	10	3L MoS ₂	2.5	2	Unknown		V-shaped gap	
	14	10	3L MoS ₂	2.9	104	None		V-shaped gap	
	16	10	3L MoS ₂	3.5	344	None			
	10	8	4L MoS ₂	1.52	408	Singlet	0.75		1d, S4
	13	6	4L MoS ₂	1.1	425	Singlet	0.67		S5
	12	8	4L MoS ₂	0.71	150	Accidental degeneracy	0.64		On NbSe ₂ edge
6	8	4L MoS ₂	1.96	554	Accidental degeneracy				
7	8	4L MoS ₂	1.6	587	Unknown				S2(c)

Details of all measured tunnel junctions (53 junctions)									
Device	Junction	NbSe ₂ thickness, nm	Tunnel barrier, layers (L)	Area of T _j um ²	G _N /G ₀	Ground state	g-factor	Comments	Figure (*in Ref. [27])
D21	9	8	4L MoS ₂	1.96	303	Unknown			
	16	6	4L MoS ₂	1.25	630	None			
	11	8	4L MoS ₂	1.56	650	Unknown			
	20	6	4L MoS ₂	1.4	920	Unknown			
	14	6	4L MoS ₂	1.49	271	None			
MN1	7	11	3L MoS ₂	1.56	826	Unknown		Partly located on the hole of MoS ₂	1b, 1c, SI
	17	11	3L MoS ₂	0.68	6	Unknown		On NbSe ₂ edge	2d blue
MN4	16	8	5L MoS ₂	3	1013	Unknown			
	15	8	5L MoS ₂	8	54	Unknown		on NbSe ₂ crystal step	
	14	8	4L MoS ₂	9.1	334	Unknown		on NbSe ₂ crystal step	
	11	10	4L MoS ₂	4.6	359	Unknown		on NbSe ₂ edge	
	3	14	5L MoS ₂	3.5	327	Unknown		on NbSe ₂ edge	2d black and red
	9	10	5L MoS ₂	6.2	52	Unknown		on NbSe ₂ edge	
	17	8	5L MoS ₂	3.64	145	Unknown		Subgap states at the gap edge	

A count of the ground states shown in Figure 5.7 summarized our measurements. More than half of tunnel junctions show subgap excitations, however many of them do not show clear behaviour under an in-plane magnetic field or suppress under a small magnetic field. From the behaviour of the rest of the tunnel junctions, we believe six tunnel junctions have singlet ground state, one - doublet, and four tunnel junctions show accidental degeneracy of a doublet and a hybridized singlet states.

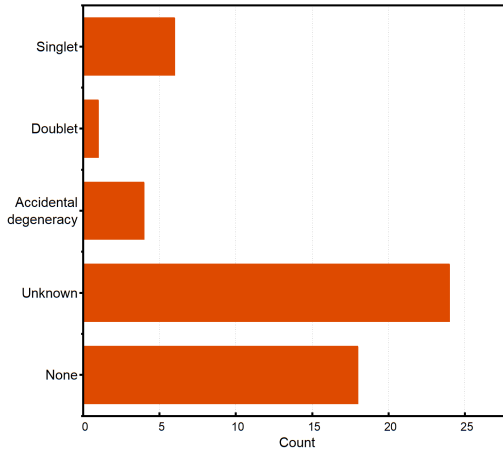


Figure 5.7 Count of ground states of observed in-gap Andreev bound states

5.4.1 Alignment of the magnetic field for the tunnel junctions with sub-gap excitations

To properly analyze the superconducting gap in the presence of a magnetic field, it is important to account for the fact that the alignment of the magnetic field is complicated by the formation of vortices in NbSe₂, a type II superconductor. This results in the compensation $B_{split-coil}$ values not increasing linearly with increasing $B_{solenoid}$ as expected.

Additionally, the data analysis for sub-gap excitations is also complicated by the need to search for the minimum of in-gap conductance and the additional

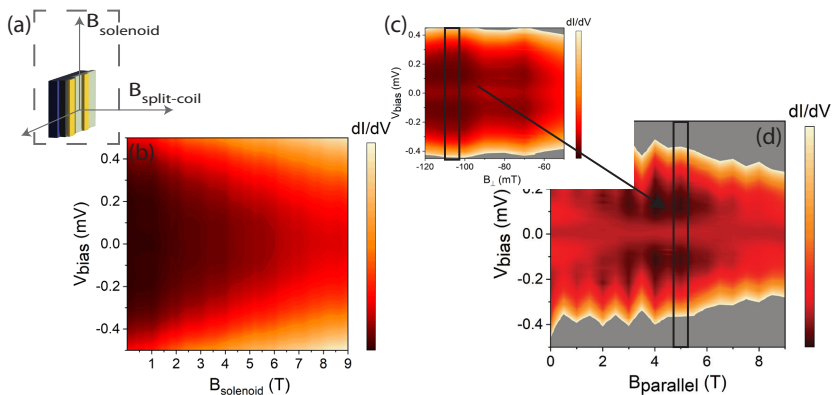


Figure 5.8 Magnetic measurement. (a) The schematic of the sample orientation with respect to the magnetic fields axis. (b) The plot shows the rise of conductance with the $B_{solenoid}$. The reason is the misalignment between the magnetic field direction and the device's plane. (c) The map is taken at constant $B_{solenoid}=5$ T. Here the tunnel junction was measured in the small range of split-coil magnetic field to obtain the spectra with the minimum of conductance, which would mean that the solenoid's magnetic field is aligned with the device. (d) The figure shows the result of proceeded data for the same tunnel junction as in (b).

alignment required to observe sub-gap excitations better. To address these issues, a process was used as follow:

1. Aligning the device perpendicularly with respect to the direction of $B_{split-coil}$, taking measurements of dI/dV vs. V_{bias} and $B_{split-coil}$ for each $B_{solenoid}$ value. Fig. 5.8 (c) shows the measurement at $B_{solenoid}=5$ T.
2. Making a profile on the obtained two-dimensional map where the in-gap conductance away from sub-gap excitation has its minimum, Fig. 5.8 (c) black frame.
3. Shifting dI/dV values for clarity of the subgap states², and combining profiles into a plot of dI/dV vs. V_{bias} and effective $B_{parallel}$, Fig. 5.8 (d).

² dI/dV values were shifted for clarity of the subgap states in such a way that all runs have the same value of conductance at zero bias

6 Conclusion and outlook

The main focus of this dissertation was to study the sub-gap excitations observed in NbSe₂-based van der Waals heterostructures. The motivation for this research was driven by the fact that NbSe₂ is known for its unconventional superconductivity[30, 32]. Because of the strong spin-orbit magnetic field pointed out-of-plane, this material is robust to external in-plane magnetic fields. Furthermore, this superconductor has a relatively large superconducting gap, approximately 1.1 meV at 255 mK. The research in this thesis was conducted by studying different tunneling heterostructure designs in order to uncover the origin of these excitations.

The fabrication process and measurement set-up used for the projects in this thesis were described in Chapter 3. In Chapter 4, we analyzed macroscopic parameters such as the critical transition temperature (T_c) and upper critical magnetic field values to characterize the properties of NbSe₂. For 17 nm NbSe₂ flake $T_c \approx 6$ K, the critical perpendicular to the flake magnetic field at $T=1.6$ K is around 3.5 T. We explain this by the influence of the orbital effect. The low-temperature measurements (at $T=255$ mK) are provided only for tunneling NbSe₂-MoS₂ devices with NbSe₂ thickness around 10 nm. At 4 T of the perpendicular magnetic field, the superconducting gap shows significant suppression, while at 9 T of the in-plane magnetic field, which is the limit of the cryostat, the superconducting gap remains the same. In the case of the in-plane magnetic field, we explain the data by the absence of orbital effect, but also due to the presence of spin-orbit coupling since without it the upper critical magnetic field would be equal to around 10.5 T (Pauli limit, H_p).

We examined our tunneling junctions by finding the suppression factor G_N/G_0 , which is for most of the tunnel junctions¹ is more than 100. Additionally, by estimating of transparency of the tunneling barrier, we can conclude that we have high-quality tunnel junctions. Using different models, we determined that the superconducting gap of NbSe₂ is composed of two types of bands, which is in agreement with previous researches[50, 56].

In Chapter 5, our research focused on sub-gap excitations. It demonstrated that NbSe₂ edges contain numerous defect states strongly coupled to the superconductor and forming Andreev bound states. The isolation of the NbSe₂ edge revealed that sub-gap states occur in MoS₂ tunnel barriers but are not

¹See the table of all tunnel junctions in Sec.5.4.3.

found in hBN tunnel barriers, indicating defects in MoS₂ are the probable cause. The magnetic measurement allows determining the type of the quantum dot-like defect's ground state by observing the doublet's Zeeman splitting. We typically observed a singlet ground state; however, some spectra showed avoided crossings of sub-gap excitations, indicating the importance of strong spin-orbit coupling in the heterostructures.

A particular interest of Andreev bound states (ABS) is that they provide a mechanism for exchanging Cooper pairs between quantum dots and superconductors, which would otherwise be impossible due to the single electron nature of quantum dots and the superconductor's Cooper pair transport. Furthermore, due to the strong coherent coupling of ABS with a superconductor, it allows for the manipulation and measuring of ABS, which makes them very prominent for the quantum computing application[2]. It is also very important to note that Andreev bound states can be reliably observed in a wide range of nanoscale device geometries, including nanowires and two-dimensional systems.

As a next step, creating NbSe₂ thin films with minimum defects on the edges would be necessary to observe the predicted topological superconductivity. However, this also requires a very high in-plane magnetic field, higher than $3H_p$, which corresponds to more than 17 T for 3 nm NbSe₂. In addition, it would be interesting to investigate superconductivity in twisted bilayer graphene and other unconventional superconducting vdW systems using the high quality of vdW tunnel junctions.

7 Appendix

7.1 Exfoliation

7.1.1 Material sources

- NbSe₂: bulk 2H-NbSe₂ is provided by Helmuth Berger and Laszlo Forro from EPFL
- Graphite: NGS Trading and Consulting GmbH, natural graphite source
- MoS₂: SPI supplies MoS₂ single crystal medium
- hBN: T. Taniguchi et al., National Institute for Material Science, 1-1 Namiki, Tsukuba 305-0044, Japan
- Exfoliation tape: NITTO ELP BT-150P-LC
- PDMS: Gel-pak n.4

7.1.2 Stacking

PC solution:

1. to add 0.6-0.8 g of Poly(Bisphenol A carbonate) (Aldrich company) and 20 ml of chloroform in the beaker with the lead.
2. let the solution to be stirred for more than 8 hours at 40°C to dissolve the PC. Put around the lead the parafilm to minimise the chloroform evaporation

7.2 Fabrication contacts by electron beam lithography

PMMA mask for contact deposition

1. The solution for the e-beam resist: PMMA 950k in Anisole (solid content of 4.5-5.5 percent)
2. Spin coating at 4000 rpm for 40s with ramp rate of 1000rpm/s (around 430 nm)

3. Baking at 180°C for 3 min
4. Exposing with e-beam (EHT=20 kV; dose=430 $\mu\text{C}/\text{cm}^2$)
5. Development in cold mixture of (around 10°C) IPA:H₂O (7:3) for 60 seconds
6. Blow drying with N₂ gun

Metal deposition

1. Prepare PMMA mask, see the section above
2. Oxygen plasma (power 30 W, pressure 250 mTorr, time 30 s) was used for the bonding places, for tunnel junctions no etching allowed
3. To deposit the metal a Sharon e-beam evaporator was used
4. Deposition of a sticking layer: 5 nm of Ti
5. Evaporation of Au, usually around 60 nm
6. Lift-off in Acetone: put sample in acetone for 1 h at room temperature to dissolve PMMA, by flow created with a syringe remove remaining metal, put the sample in IPA for 3 min, dry with N₂ gun

Bibliography

- [1] T. D. Ladd, F. Jelezko, R. Laflamme, Y. Nakamura, C. Monroe, and J. L. O'Brien, "Quantum computers," *nature*, vol. 464, no. 7285, pp. 45–53, 2010.
- [2] A. Zazunov, V. Shumeiko, E. Bratus, J. Lantz, and G. Wendin, "Andreev level qubit," *Physical review letters*, vol. 90, no. 8, p. 087003, 2003.
- [3] K. S. Novoselov, A. K. Geim, S. V. Morozov, D.-e. Jiang, Y. Zhang, S. V. Dubonos, I. V. Grigorieva, and A. A. Firsov, "Electric field effect in atomically thin carbon films," *science*, vol. 306, no. 5696, pp. 666–669, 2004.
- [4] L. D. Landau, "On the theory of phase transitions. i.," *Zh. Eksp. Teor. Fiz.*, vol. 11, p. 19, 1937.
- [5] A. K. Geim and I. V. Grigorieva, "Van der waals heterostructures," *Nature*, vol. 499, no. 7459, pp. 419–425, 2013.
- [6] H. K. Onnes, *Communications from the Physical Laboratory at the University of Leiden*. No. 145-156, The University, 1922.
- [7] M. Tinkham, *Introduction to Superconductivity*, vol. 2. Dover, 1996.
- [8] S. De Franceschi, L. Kouwenhoven, C. Schönberger, and W. Wernsdorfer, "Hybrid superconductor–quantum dot devices," *Nature nanotechnology*, vol. 5, no. 10, pp. 703–711, 2010.
- [9] J. Bardeen, L. Cooper, and J. Schrieffer, "Theory of superconductivity," *Physical Review*, vol. 108, no. 5, p. 1175, 1957.
- [10] T. T. Heikkilä, *The Physics of Nanoelectronics: Transport and Fluctuation Phenomena at Low Temperatures*. Oxford University Press, 2011.
- [11] M. Tinkham, *Introduction to Superconductivity*. Courier Corporation, 2004.
- [12] S. d'Hollosy, *Locally Tunable InAs Nanowire Quantum Dots for Cooper Pair Splitting*. PhD thesis, University of Basel, 2014.

- [13] N. W. Ashcroft, “Solid state physics (hr&w) google scholar nw ashcroft and nd mermin 1979,” *Solid State Physics*, vol. 1, p. 2, 1976.
- [14] A. Bordoloi, V. Zannier, L. Sorba, C. Schönenberger, and A. Baumgartner, “Spin cross-correlation experiments in an electron entangler,” *Nature*, vol. 612, no. 7940, pp. 454–458, 2022.
- [15] D. Indolese, *Engineered graphene Josephson junctions probed by quantum interference effects*. PhD thesis, University_of_Basel, 2021.
- [16] A. M. Forrest, “Meissner and ochsenfeld revisited,” *European Journal of Physics*, vol. 4, no. 2, p. 117, 1983.
- [17] C. Sergio, M. R. Sinko, D. P. Gopalan, N. Sivadas, K. L. Seyler, K. Watanabe, T. Taniguchi, A. W. Tsun, X. Xu, D. Xiao, *et al.*, “Tuning ising superconductivity with layer and spin–orbit coupling in two-dimensional transition-metal dichalcogenides,” *Nature communications*, vol. 9, no. 1, pp. 1–8, 2018.
- [18] T. Ihn, *Electronic quantum transport in mesoscopic semiconductor structures*, vol. 192. Springer, 2004.
- [19] J. Schindele, *Observation of Cooper Pair Splitting and Andreev Bound States in Carbon Nanotubes*. PhD thesis, University of Basel, 2014.
- [20] S. Hollosy, *Locally tunable inAs nanowire quantum dots for cooper pair splitting*. PhD thesis, University_of_Basel, 2014.
- [21] J. Bauer, A. Oguri, and A. Hewson, “Spectral properties of locally correlated electrons in a bardeen–cooper–schrieffer superconductor,” *Journal of Physics: Condensed Matter*, vol. 19, no. 48, p. 486211, 2007.
- [22] H. Huang, C. Padurariu, J. Senkpiel, R. Drost, A. L. Yeyati, J. C. Cuevas, B. Kubala, J. Ankerhold, K. Kern, and C. R. Ast, “Tunnelling dynamics between superconducting bound states at the atomic limit,” *Nature Physics*, vol. 16, no. 12, pp. 1227–1231, 2020.
- [23] J. Schindele, A. Baumgartner, R. Maurand, M. Weiss, and C. Schönenberger, “Nonlocal spectroscopy of andreev bound states,” *Physical Review B*, vol. 89, no. 4, p. 045422, 2014.
- [24] S. A. González, L. Melischek, O. Peters, K. Flensberg, K. J. Franke, and F. von Oppen, “Photon-assisted resonant andreev reflections: Yu-shiba-rusinov and majorana states,” *Physical Review B*, vol. 102, no. 4, p. 045413, 2020.

- [25] A. Martín-Rodero and A. Levy Yeyati, “Josephson and andreev transport through quantum dots,” *Advances in Physics*, vol. 60, no. 6, pp. 899–958, 2011.
- [26] A. Braggio, M. Governale, M. G. Pala, and J. König, “Superconducting proximity effect in interacting quantum dots revealed by shot noise,” *Solid State Communications*, vol. 151, no. 2, pp. 155–158, 2011.
- [27] P. Karnatak, Z. Mingazheva, K. Watanabe, T. Taniguchi, H. Berger, L. Forró, and C. Schönenberger, “Origin of subgap states in normal-insulator-superconductor van der waals heterostructures,” *arXiv preprint arXiv:2207.05741*, 2022.
- [28] I. Giaever, “Electron tunneling between two superconductors,” *Physical Review Letters*, vol. 5, no. 10, p. 464, 1960.
- [29] D. Moncton, J. Axe, and F. DiSalvo, “Study of superlattice formation in 2 h-nb se 2 and 2 h-ta se 2 by neutron scattering,” *Physical Review Letters*, vol. 34, no. 12, p. 734, 1975.
- [30] X. Xi, Z. Wang, W. Zhao, J.-H. Park, K. T. Law, H. Berger, L. Forró, J. Shan, and K. F. Mak, “Ising pairing in superconducting NbSe₂ atomic layers,” *Nature Physics*, vol. 12, no. 2, pp. 139–143, 2016.
- [31] D. Möckli and M. Khodas, “Robust parity-mixed superconductivity in disordered monolayer transition metal dichalcogenides,” *Physical Review B*, vol. 98, no. 14, p. 144518, 2018.
- [32] S. C. Barrera, M. R. Sinko, D. P. Gopalan, N. Sivadas, K. L. Seyler, K. Watanabe, T. Taniguchi, A. W. Tsun, X. Xu, D. Xiao, *et al.*, “Tuning ising superconductivity with layer and spin-orbit coupling in two-dimensional transition-metal dichalcogenides,” *Nature communications*, vol. 9, no. 1, pp. 1–8, 2018.
- [33] M. Ramezani, I. C. Sampaio, K. Watanabe, T. Taniguchi, C. Schonenberger, and A. Baumgartner, “Superconducting contacts to a monolayer semiconductor,” *Nano Letters*, vol. 21, no. 13, pp. 5614–5619, 2021.
- [34] R. A. Doganov, E. C. O’farrell, S. P. Koenig, Y. Yeo, A. Ziletti, A. Carvalho, D. K. Campbell, D. F. Coker, K. Watanabe, T. Taniguchi, *et al.*, “Transport properties of pristine few-layer black phosphorus by van der waals passivation in an inert atmosphere,” *Nature communications*, vol. 6, no. 1, pp. 1–7, 2015.
- [35] A. Splendiani, L. Sun, Y. Zhang, T. Li, J. Kim, C.-Y. Chim, G. Galli, and F. Wang, “Emerging photoluminescence in monolayer mos₂,” *Nano letters*, vol. 10, no. 4, pp. 1271–1275, 2010.

- [36] K. F. Mak, C. Lee, J. Hone, J. Shan, and T. F. Heinz, “Atomically thin mos 2: a new direct-gap semiconductor,” *Physical review letters*, vol. 105, no. 13, p. 136805, 2010.
- [37] G. Cassabois, P. Valvin, and B. Gil, “Hexagonal boron nitride is an indirect bandgap semiconductor,” *Nature photonics*, vol. 10, no. 4, pp. 262–266, 2016.
- [38] Y. Zhang, Y.-W. Tan, H. L. Stormer, and P. Kim, “Experimental observation of the quantum hall effect and berry’s phase in graphene,” *nature*, vol. 438, no. 7065, pp. 201–204, 2005.
- [39] B. Radisavljevic, A. Radenovic, J. Brivio, V. Giacometti, and A. Kis, “Single-layer mos2 transistors,” *Nature nanotechnology*, vol. 6, no. 3, pp. 147–150, 2011.
- [40] R. V. Gorbachev, I. Riaz, R. R. Nair, R. Jalil, L. Britnell, B. D. Belle, E. W. Hill, K. S. Novoselov, K. Watanabe, T. Taniguchi, *et al.*, “Hunting for monolayer boron nitride: optical and raman signatures,” *Small*, vol. 7, no. 4, pp. 465–468, 2011.
- [41] Z. Hu, Z.-B. Liu, and J.-G. Tian, “Stacking of exfoliated two-dimensional materials: a review,” *Chinese Journal of Chemistry*, vol. 38, no. 9, pp. 981–995, 2020.
- [42] L. Wang, I. Meric, P. Huang, Q. Gao, Y. Gao, H. Tran, T. Taniguchi, K. Watanabe, L. Campos, D. Muller, *et al.*, “One-dimensional electrical contact to a two-dimensional material,” *Science*, vol. 342, no. 6158, pp. 614–617, 2013.
- [43] P. Zomer, M. Guimarães, J. Brant, N. Tombros, and B. Van Wees, “Fast pick up technique for high quality heterostructures of bilayer graphene and hexagonal boron nitride,” *Applied Physics Letters*, vol. 105, no. 1, p. 013101, 2014.
- [44] T. Heinzl, *Mesoscopic electronics in solid state nanostructures*. John Wiley & Sons, 2008.
- [45] H. Bluhm and K. A. Moler, “Dissipative cryogenic filters with zero dc resistance,” *Review of Scientific Instruments*, vol. 79, no. 1, p. 014703, 2008.
- [46] S. Zihlmann, *Spin and charge relaxation in graphene*. PhD thesis, University_of_Basel, 2018.

- [47] X. Xi, L. Zhao, Z. Wang, H. Berger, L. Forró, J. Shan, and K. F. Mak, “Strongly enhanced charge-density-wave order in monolayer nbse2,” *Nature nanotechnology*, vol. 10, no. 9, pp. 765–769, 2015.
- [48] Y. Sata, R. Moriya, N. Yabuki, S. Masubuchi, and T. Machida, “Heat transfer at the van der waals interface between graphene and nbse 2,” *Physical Review B*, vol. 98, no. 3, p. 035422, 2018.
- [49] R. Pervin, M. Krishnan, A. K. Rana, M. Kannan, S. Arumugam, and P. M. Shirage, “Enhancement of superconducting critical current density by fe impurity substitution in nbse 2 single crystals and the vortex pinning mechanism,” *Physical Chemistry Chemical Physics*, vol. 19, no. 18, pp. 11230–11238, 2017.
- [50] T. Dvir, F. Masee, L. Attias, M. Khodas, M. Aprili, C. H. Quay, and H. Steinberg, “Spectroscopy of bulk and few-layer superconducting nbse2 with van der waals tunnel junctions,” *Nature communications*, vol. 9, no. 1, pp. 1–6, 2018.
- [51] Y. V. Sharvin, “On the possible method for studying fermi surfaces,” *Zh. Eksperim. i Teor. Fiz.*, vol. 48, 1965.
- [52] I. Mazin, “Tunneling of bloch electrons through vacuum barrier,” *EPL (Europhysics Letters)*, vol. 55, no. 3, p. 404, 2001.
- [53] E. Khestanova, J. Birkbeck, M. Zhu, Y. Cao, G. Yu, D. Ghazaryan, J. Yin, H. Berger, L. Forro, T. Taniguchi, *et al.*, “Unusual suppression of the superconducting energy gap and critical temperature in atomically thin nbse2,” *Nano letters*, vol. 18, no. 4, pp. 2623–2629, 2018.
- [54] Y. Noat, J. A. Silva-Guillén, T. Cren, V. Cherkez, C. Brun, S. Pons, F. Debontridder, D. Roditchev, W. Sacks, L. Cario, *et al.*, “Quasiparticle spectra of 2 h- nbse 2: Two-band superconductivity and the role of tunneling selectivity,” *Physical Review B*, vol. 92, no. 13, p. 134510, 2015.
- [55] N. Hayashi, M. Ichioka, and K. Machida, “Star-shaped local density of states around vortices in a type-ii superconductor,” *Physical review letters*, vol. 77, no. 19, p. 4074, 1996.
- [56] T. Yokoya, T. Kiss, A. Chainani, S. Shin, M. Nohara, and H. Takagi, “Fermi surface sheet-dependent superconductivity in 2 h-nbse2,” *Science*, vol. 294, no. 5551, pp. 2518–2520, 2001.
- [57] M. Johannes, I. Mazin, and C. Howells, “Fermi-surface nesting and the origin of the charge-density wave in nb se 2,” *Physical Review B*, vol. 73, no. 20, p. 205102, 2006.

- [58] H. Boschker, E. Fillis-Tsirakis, C. Richter, D. Zhang, J. Smet, and L. Kuerten, “Microscopic origin of the dynes parameter γ of the laalo 3–srtio 3 interface superconductor,” *Physical Review B*, vol. 102, no. 13, p. 134506, 2020.
- [59] W.-Y. He, B. T. Zhou, J. J. He, N. F. Yuan, T. Zhang, and K. T. Law, “Magnetic field driven nodal topological superconductivity in monolayer transition metal dichalcogenides,” *Communications Physics*, vol. 1, no. 1, pp. 1–7, 2018.
- [60] J. Lu, O. Zheliuk, I. Leermakers, N. F. Yuan, U. Zeitler, K. T. Law, and J. Ye, “Evidence for two-dimensional ising superconductivity in gated MoS₂,” *Science*, vol. 350, no. 6266, pp. 1353–1357, 2015.
- [61] Y. Yang, S. Fang, V. Fatemi, J. Ruhman, E. Navarro-Moratalla, K. Watanabe, T. Taniguchi, E. Kaxiras, and P. Jarillo-Herrero, “Enhanced superconductivity upon weakening of charge density wave transport in 2H-TaS₂ in the two-dimensional limit,” *Physical Review B*, vol. 98, no. 3, p. 035203, 2018.
- [62] D. Shaffer, J. Kang, F. J. Burnell, and R. M. Fernandes, “Crystalline nodal topological superconductivity and bogolyubov fermi surfaces in monolayer NbSe₂,” *Phys. Rev. B*, vol. 101, p. 224503, Jun 2020.
- [63] J. Schindele, A. Baumgartner, and C. Schönenberger, “Near-unity cooper pair splitting efficiency,” *Physical review letters*, vol. 109, no. 15, p. 157002, 2012.
- [64] M. Buitelaar, T. Nussbaumer, and C. Schönenberger, “Quantum dot in the kondo regime coupled to superconductors,” *Physical Review Letters*, vol. 89, no. 25, p. 256801, 2002.
- [65] E. J. Lee, X. Jiang, M. Houzet, R. Aguado, C. M. Lieber, and S. De Franceschi, “Spin-resolved andreev levels and parity crossings in hybrid superconductor–semiconductor nanostructures,” *Nature nanotechnology*, vol. 9, no. 1, pp. 79–84, 2014.
- [66] R. M. Lutchyn, J. D. Sau, and S. D. Sarma, “Majorana fermions and a topological phase transition in semiconductor-superconductor heterostructures,” *Physical review letters*, vol. 105, no. 7, p. 077001, 2010.
- [67] Y. Oreg, G. Refael, and F. Von Oppen, “Helical liquids and majorana bound states in quantum wires,” *Physical review letters*, vol. 105, no. 17, p. 177002, 2010.

- [68] T. Dvir, M. Aprili, C. H. L. Quay, and H. Steinberg, “Zeeman tunability of andreev bound states in van der waals tunnel barriers,” *Phys. Rev. Lett.*, vol. 123, p. 217003, Nov 2019.
- [69] T. Devidas, I. Keren, and H. Steinberg, “Spectroscopy of NbSe₂ using energy-tunable defect-embedded quantum dots,” *Nano Letters*, vol. 21, no. 16, pp. 6931–6937, 2021.
- [70] G. C. Ménard, S. Guissart, C. Brun, S. Pons, V. S. Stolyarov, F. Debontridder, M. V. Leclerc, E. Janod, L. Cario, D. Roditchev, *et al.*, “Coherent long-range magnetic bound states in a superconductor,” *Nature Physics*, vol. 11, no. 12, pp. 1013–1016, 2015.
- [71] S. Kezilebieke, M. Dvorak, T. Ojanen, and P. Liljeroth, “Coupled yu-shiba-rusinov states in molecular dimers on NbSe₂,” *Nano letters*, vol. 18, no. 4, pp. 2311–2315, 2018.
- [72] E. Liebhaber, S. Acero Gonzalez, R. Baba, G. Reece, B. W. Heinrich, S. Rohlf, K. Rossnagel, F. von Oppen, and K. J. Franke, “Yu–shiba–rusinov states in the charge-density modulated superconductor NbSe₂,” *Nano letters*, vol. 20, no. 1, pp. 339–344, 2019.
- [73] T. Taniguchi and K. Watanabe, “Synthesis of high-purity boron nitride single crystals under high pressure by using ba–bn solvent,” *Journal of crystal growth*, vol. 303, no. 2, pp. 525–529, 2007.
- [74] L. Yu, “Bound state in superconductors with paramagnetic impurities,” *Acta Phys. Sin.*, vol. 21, no. 1, p. 75, 1965.
- [75] H. Shiba, “Classical spins in superconductors,” *Progress of theoretical Physics*, vol. 40, no. 3, pp. 435–451, 1968.
- [76] A. Rusinov, “Superconductivity near a paramagnetic impurity,” *JETP Lett. (USSR)(Engl. Transl.); (United States)*, vol. 9, 1969.
- [77] S. Kezilebieke, M. N. Huda, V. Vaño, M. Aapro, S. C. Ganguli, O. J. Silveira, S. Głódzik, A. S. Foster, T. Ojanen, and P. Liljeroth, “Topological superconductivity in a van der waals heterostructure,” *Nature*, vol. 588, no. 7838, pp. 424–428, 2020.
- [78] U. Chandni, K. Watanabe, T. Taniguchi, and J. Eisenstein, “Evidence for defect-mediated tunneling in hexagonal boron nitride-based junctions,” *Nano letters*, vol. 15, no. 11, pp. 7329–7333, 2015.

- [79] H. Qiu, T. Xu, Z. Wang, W. Ren, H. Nan, Z. Ni, Q. Chen, S. Yuan, F. Miao, F. Song, *et al.*, “Hopping transport through defect-induced localized states in molybdenum disulphide,” *Nature communications*, vol. 4, no. 1, pp. 1–6, 2013.
- [80] Z. Yu, Y. Pan, Y. Shen, Z. Wang, Z.-Y. Ong, T. Xu, R. Xin, L. Pan, B. Wang, L. Sun, *et al.*, “Towards intrinsic charge transport in monolayer molybdenum disulfide by defect and interface engineering,” *Nature communications*, vol. 5, no. 1, pp. 1–7, 2014.
- [81] J. Hong, Z. Hu, M. Probert, K. Li, D. Lv, X. Yang, L. Gu, N. Mao, Q. Feng, L. Xie, *et al.*, “Exploring atomic defects in molybdenum disulphide monolayers,” *Nature communications*, vol. 6, no. 1, pp. 1–8, 2015.
- [82] P. Vancsó, G. Z. Magda, J. Pető, J.-Y. Noh, Y.-S. Kim, C. Hwang, L. P. Biró, and L. Tapasztó, “The intrinsic defect structure of exfoliated MoS₂ single layers revealed by scanning tunneling microscopy,” *Scientific reports*, vol. 6, no. 1, pp. 1–7, 2016.
- [83] M. W. De Moor, J. D. Bommer, D. Xu, G. W. Winkler, A. E. Antipov, A. Bargerbos, G. Wang, N. Van Loo, R. L. O. het Veld, S. Gazibegovic, *et al.*, “Electric field tunable superconductor-semiconductor coupling in majorana nanowires,” *New Journal of Physics*, vol. 20, no. 10, p. 103049, 2018.
- [84] C. Fasth, A. Fuhrer, L. Samuelson, V. N. Golovach, and D. Loss, “Direct measurement of the spin-orbit interaction in a two-electron inas nanowire quantum dot,” *Physical review letters*, vol. 98, no. 26, p. 266801, 2007.
- [85] E. O’Farrell, A. Drachmann, M. Hell, A. Fornieri, A. Whiticar, E. Hansen, S. Gronin, G. Gardner, C. Thomas, M. Manfra, *et al.*, “Hybridization of subgap states in one-dimensional superconductor-semiconductor coulomb islands,” *Physical review letters*, vol. 121, no. 25, p. 256803, 2018.

Curriculum Vitae

Zarina Mingazheva Born on 29th April, 1994, in Russia

Education

11/2018-02/2023 **PhD in Experimental Physics at the University of Basel, Switzerland**

- Dissertation in the group of Prof. Dr. Christian Schö-
nenberger
*“Exploring bound states of NbSe₂ van der Waals su-
perconductor probed by tunneling spectroscopy”*

09/2016 – 06/2018 **Master of Nanotechnology and Microsystem en-
gineering at NUST “MISiS”, Department of Tech-
nologies of Electronic Materials, Russia**

- Master thesis *“Development of sample holders for mi-
crowave spectroscopy of superconducting metamateri-
als and investigation of electronic properties of a high-
temperature superconductor La_{1.78}Sr_{0.22}CuO₄”*

09/2012-07/2016 **Bachelor of Nanotechnology and Microsystem en-
gineering at NUST “MISiS”, Department of Tech-
nologies of Electronic Materials, Russia**

- Bachelor thesis *“Electrophysical characteristics of a
composite F42 polymer/ ferrite 2000 NM, fabrication
and research.”*

Positions

02/2019-12/2022 Teaching assistant for physics at the University of Basel

Publications

- “*Origin of subgap states in normal-insulator-superconductor van der Waals heterostructures*”
P.Karnatak, **Z.Mingazheva**, K. Watanabe, T. Taniguchi, H. Berger, L. Forro, C. Schönenberger
[Nano Letters 2023, 23, 7, 2454-2459](#)

Acknowledgements

Looking back on this intensive and wonderful period of my life, I am deeply grateful to all the people who have supported me throughout my Ph.D. journey.

First, I want to thank Prof. Dr. Christian Schönenberger for giving me the opportunity to carry out my Ph.D. work in his group. His great passion for nanoelectronics and active engagement in all of our group's projects gave me additional charge and motivation to study such a complicated field. His excellent leadership created the ideal conditions for conducting experiments under his supervision. I am truly grateful for his belief in me, his support, and the wonderful discussions and feedback during our meetings, which helped me a lot in understand many complex topics.

I would like to thank my second supervisor, Prof. Dr. Ernst Meyer, for our meetings, his interest, and his thoughtful feedback on my projects. I would also like to thank Dr. Oliver Gröning for his time and effort in reading and evaluating my thesis and for taking part in my doctoral committee.

I would like to express my sincere thanks to our entire amazing Quantum and Nanoelectronics group. It was a great pleasure to work in such a friendly and supportive team. I also greatly cherish the memories of our fantastic team events, where we had many great moments and got to know each other better. I am incredibly grateful for the collaboration with my postdoc, Dr. Paritosh Karnatak, for sharing his deep knowledge and extensive experience in nanofabrication and electronics, supervising me in a complicated project, and for his very friendly and supportive personality. I am also thankful to Artem Kononov and Martin Endres; it was an honor for me to join their discussions at times, and I would also like to thank them for their valuable feedback on parts of my thesis. I am thankful to Andreas Baumgartner for the project discussions and feedback on my work. I am also grateful to Alessia Pally for being such a great and supportive colleague.

I want to extend my gratitude to Barbara Kammerman for her help with bureaucracy, Dominic Suffergier for providing helium, and the electronics workshop for their work in making I/V converters, filters, and other electronic components.

I would like to thank Valentin Kochervinskii and Aleksandar Morchenko, with whom I first became involved in science during my bachelor's study. I will always also cherish the memories of our classical concerts together. I

would also like to thank Prof. Johan Chang and Dr. Nicholas Plumb for the amazing opportunities to conduct internships in their group, which gave me the courage to start my Ph.D.

I am deeply grateful to my family for their love and support in all situations. I am thankful so much to my mother, Zoia Mingazheva, for her big love and support of me and my sister. I am also thankful for her prioritizing our education. I am greatly thankful to my sister, Rizalina Mingazheva. Her bright example, belief in me, and great advice helped me greatly to achieve many goals and gave me the courage to start to go my own way. I am very thankful to my husband, Till Vontobel, for his love, support, and stability. I am also thankful to him for supporting me in my achievements in different aspects, from listening to me and offering thoughtful advice to organizing a great apero for the celebration of my defense.

Thank you!